PEG-templated synthesis of ultramicroporous n-ZIF-67 nanoparticles with high selectivity for the adsorption and uptake of CO2 over CH4 and N2

Nadhem Missaoui, Amani Chrouda, Hamza Kahri, Andrew James Gross, Mohammad Rezaei Ardani, Ai Ling Pang, Mohsen Ahmadipour

PEG-templated synthesis of ultramicroporous n-ZIF-67 nanoparticles with high selectivity for the adsorption and uptake of CO_2 over CH_4 and N_2

Nadhem Missaoui[1*], Amani Chrouda[2,3*], Hamza Kahri[1,4], Andrew J. Gross[5], Mohammad Rezaei Ardani[6], Pang Ai Ling[7,8*], Mohsen Ahmadipour[9*]

[1] Laboratory of Interfaces and Advanced Materials, Faculty of Sciences, University of Monastir, Tunisia
[2]Departement of Chemistry, College of Science at Zulfi, Majmaah University, Zulfi 11952, Saudi Arabia
[3]Institut de Recherche sur l'Hydrogène, Université du Québec à Trois-Rivières, 3351, Boul. des Forges, C.P.500, Trois-Rivières (QC), Canada G9A5H7.
[4]Université de Poitiers, IC2MP UMR 7285 CNRS, 86073 09 Poitiers Cedex, France
[5]Département de Chimie Moléculaire (DCM), Univ. Grenoble Alpes-CNRS, 570 rue de la chimie, 38041 Grenoble, France.
[5]School of Materials and Mineral Resources Engineering, Universiti Sains Malaysia, Engineering Campus, 14300, Nibong Tebal, Pulau Pinang, Malaysia
[7]Department of Chemical Science, Faculty of Science, Universiti Tunku Abdul Rahman, Kampar, Perak, 31900, Malaysia
[8]Centre for Photonics and Advanced Materials Research, Universiti Tunku Abdul Rahman, Sungai Long Campus, Jalan Sungai Long, Bandar Sungai Long, Cheras, 43000 Kajang, Selangor, Malaysia
[6]Institute of Microengineering and Nanoelectronics, Universiti Kebangsaan Malaysia, 43600 Bangi, Selangor, Malaysia
*Corresponding author: mahmadipour@ukm.edu.my

Abstract

Challenges remain concerning the development of rapid and low-cost adsorbents that combine good separation performance with high adsorption capacity, especially for CO_2. Herein, we report for the first time a new polyethylene glycol templated synthesis method to obtain a nanocrystalline zeolitic imidazolate framework (n-ZIF-67) at room temperature in 5 minutes. The n-ZIF-67 nanoparticles were characterized using X-ray powder diffraction with Rietveld refinement (space group = I-43 m, a = 17.0545(4) Å), Fourier-transform infrared, transmission electron microscopy, thermogravimetric analysis, and N_2 adsorption (Brunauer-Emmett-Teller) measurements and exhibited excellent properties, including a total pore volume of 0.86 cm^3/g, a high surface area equal to 1891 m^2/g, and 0.64 nm size ultramicropores.). The highly porous ZIF-67 nanoparticles were explored for the adsorption and desorption of CH_4, CO_2, and N_2 gases at pressures up to 40 bar and isotherm temperatures of 273, 298, 323, and 353 K. The adsorption isotherms revealed a high capacity for CO_2 of 681 mg/g at 298 K and an adsorption enthalpy of 29.19 to 34.44 KJ/mol, in part linked to the ultramicroporous structure. The n-ZIF-67 particles exhibited gas uptake values for CH_4 and N_2 of 241 mg/g and 219 mg/g, respectively. As far as the authors are concerned, these are the highest capacities ever reported for zeolitic framework metal organic frameworks such as ZIF-67 and ZIF-8. The Langmuir adsorption isotherm was employed to obtain the maximum adsorption capacity, q_m, and adsorption equilibrium constant, K_L. The isosteric heat of adsorption data sheds light on a CO_2 physisorption process. The n-ZIF-67 also exhibited high CO_2/N_2 and CO_2/CH_4 mixed gases selectivity, with the preferential adsorption of CO_2 over N_2 or CH_4 confirmed by breakthrough experiments. The n-ZIF-67 with ultramicropores is therefore an effective new adsorbent for greenhouse gas capture with high CO_2 gas selectivity over competing gases. Zeolitic framework MOFs merit further development as low-cost and easy-to-synthesize adsorbents to help address the pressing need to mitigate CO_2 emissions.

Keywords
Gas Adsorption; Equilibrium; Carbon dioxide; Methane; Specific Surface Area; Zeolitic Imidazolate Framework; Selectivity.

1. Introduction

One of the biggest issues facing the world community is climate change brought on by global warming. The generation and accumulation of greenhouse gases in the atmosphere have mostly been caused by the emission of gases like methane (CH_4), carbon dioxide (CO_2), and nitrogen oxide (NO_2), and especially CO_2 [1-3]. The major industrial technologies used over the past few decades for separating and capturing CO_2 and CH_4 are, in general, based on absorption by solvents, membrane separation, and adsorption methods [4-6].

Adsorbents such as activated carbon and zeolites are among the most effective materials for gas separation in the chemical industry. Thanks to their large specific surface areas and pore volumes, crystalline porous metal-organic frameworks (MOFs) show great performance for gas adsorption and storage applications. MOFs are comprised of unique networks of metal ions or clusters that are coupled to organic ligands that give rise to unprecedented chemical and structure tunability. Numerous MOFs have been formed and investigated to date for CO_2 capture, CH_4 storage, and gas mixtures separation [7, 8]. MOFs can selectively adsorb gases owing to their unique pore sizes and geometries, as well as functional groups (e.g. via electrostatics) within the pores. Zeolitic imidazolate frameworks (ZIFs) are a class of MOFs that have been used extensively and have a tetrahedral network structure that is in many ways similar to zeolites, but with the important difference that they are constructed using transition metals associated with imidazolate ligands [9]. ZIFs, notably ZIF-67, have unique chemical, thermal, and water stabilities, that makes them promising candidates for industrial adsorption applications [10, 11]. Thanks to their high specific surface and pore geometries and chemistries, ZIFs are suitable adsorbents for CO_2 and CH_4 (Table 1) [12-23].

Several methods have been reported for the production of ZIF-67 with tunable porosity and morphology, such as sol-gel, solvothermal, microwave/ultrasound-assisted, and surfactant-assisted methods [24-26]. These methods permit the preparation of highly crystalline ZIF-67 with different crystallite sizes and porosities with some control, depending on factors such as synthesis time, temperature, and solvent [22, 24, 27]. Many require reaction times of several hours to days due to slow coordination interactions and discontinuities. For example, ZIF-67 crystals are typically obtained after 12 to 72 h using solvothermal methods at temperatures between 50-200°C [25]. It is therefore desirable to not only discover high-performance adsorbent materials, but also to discover materials that can be easily, economically and ecologically obtained, with a high level of control over crystal size and morphology (including phase purity). Nanocrystalline ZIF-67 with controlled morphology and particle size can be prepared using a polymer or surfactant template [19, 23]. The use of a template can prevent the formation of non-uniform agglomerates with large variations in sample size and morphology as well as larger particles [22]. Room temperature methods capable of generating ZIF-67 in a few hours are also desirable [28]. The diverse synthesis possibilities to obtain ZIF-67 with attractive chemical and physical properties has resulted in its use as a great material for catalysis [29], separation [30], and volatile organic compounds (VOCs) adsorption [31] applications. Nevertheless, the application and advantages of ZIF-67 for gas adsorption and separation have been rarely studied (see Table 1 for a detailed literature summary).

In this study, we report the facile and fast synthesis of ZIF-67 nanoparticles (NPs) in just a few minutes using N, N-dimethylformamide (DMF) as the solvent and polyethylene glycol (PEG) as a soft template. The use of PEG with a mild reaction temperature avoids the need for conventional high temperature solvothermal and microwave methods, while promoting the formation of homogeneous and stable ZIF-67 dispersions. To the best of our knowledge, the use of PEG as a template has not been reported previously for ZIF-67 synthesis. PEG was chosen over other polymer templates since it is low cost and has the capacity to generate a homogenous mixture comprising metallic salts thanks to its attractive solubility properties. During MOF synthesis, the polymer is

considered to adsorb onto the metal surface and alter the growth kinetics of colloids, allowing for the uniform growth of hexagonally-shaped particles [19, 23]. In these former examples, poly (diallyldimethylammonium chloride) and PEG were used for the production of ZIF-67 and ZIF-8, respectively. Following successful synthesis and characterization of PEG-templated ZIF-67 nanoparticles, we report here the gravimetric adsorption studies of CO_2, CH_4, and N_2 using PEG-templated n-ZIF-67 as well as PEG-templated n-ZIF-8 as adsorbents. The adsorption/desorption isotherms were achieved at temperatures of 273, 298, 323, and 353 K, at low and high pressures, and considered together with Langmuir modelling. Real-time dynamic breakthrough experiments of PEG-templated ZIF-67 for CO_2/N_2, CO_2/CH_4 and N_2/CH_4 mixtures are also reported.

2. Material and Methods

2.1. Synthesis of PEG-templated ZIF-8 nanoparticles (n-ZIF-8)

All the materials in this study were purchased from Sigma-Aldrich and were employed as received, including cobalt nitrate hexahydrate ($Co(NO_3)\cdot 6H_2O$; 99 %), 2-methylimidazole ($C_4H_6N_2$: mIm; 99 %), N,N-dimethylformamide (DMF; 99%), polyethylene glycol (PEG, average molecular weight = 20.000 $g.mol^{-1}$), triethylamine (TEA; $(C_2H_5)_3N$; 99%), and methanol (99 %). The microporous PEG-templated ZIF-8 ($Zn(Im)_2$) nanoparticles were obtained inaccordance with the procedures of our recently reported room-temperature method [23]. The ZIF-8 material was activated under vacuum at 423 K for 12 h prior to gas adsorption measurements. Table 1 summarizes the textural properties of ZIF-8 from our previous study.

2.2. Synthesis of PEG-templated ZIF-67 nanoparticles (n-ZIF-67)

ZIF-67 NPs were synthesized in a similar manner to the previous publication with some modification [23], i.e., $Co(NO_3)_2\cdot 6H_2O$ and mIm were used as precursors with PEG as a soft template. The choice of PEG was encouraged by its ability to form a homogenous solution with metallic salts thanks to micellar and dispersion effects to promote the uniform growth of particles with reduced particle size and agglomeration. In the first step, the PEG powder (0.4 g) was dispersed in 10 mL of DMF; $Co(NO_3)_2\cdot 6H_2O$ (1.4551 g, 5 mmol) was then added with slight stirring for 2 min at 298 K to form the Co-solution. Later, 2-methylimidazole (2.0525 g, 25 mmol) was dispersed in DMF (10 mL); TEA was used as a base and slowly added (6.75 mL) with stirring over 3 min to obtain the linker-solution. After complete dissolution, the Co-solution was mixed with the linker-solution and stirred for 5 min at room temperature. The purple precipitates were filtered, washed with ethanol to remove possible undissolved reagents including PEG, then collected via centrifugation (4000 rpm, 10 min). Finally, the obtained purple powder was dried in a vacuum oven at 423 K for 24 h to achieve the final product, ZIF-67 NP (herein referred to as n-ZIF-67).

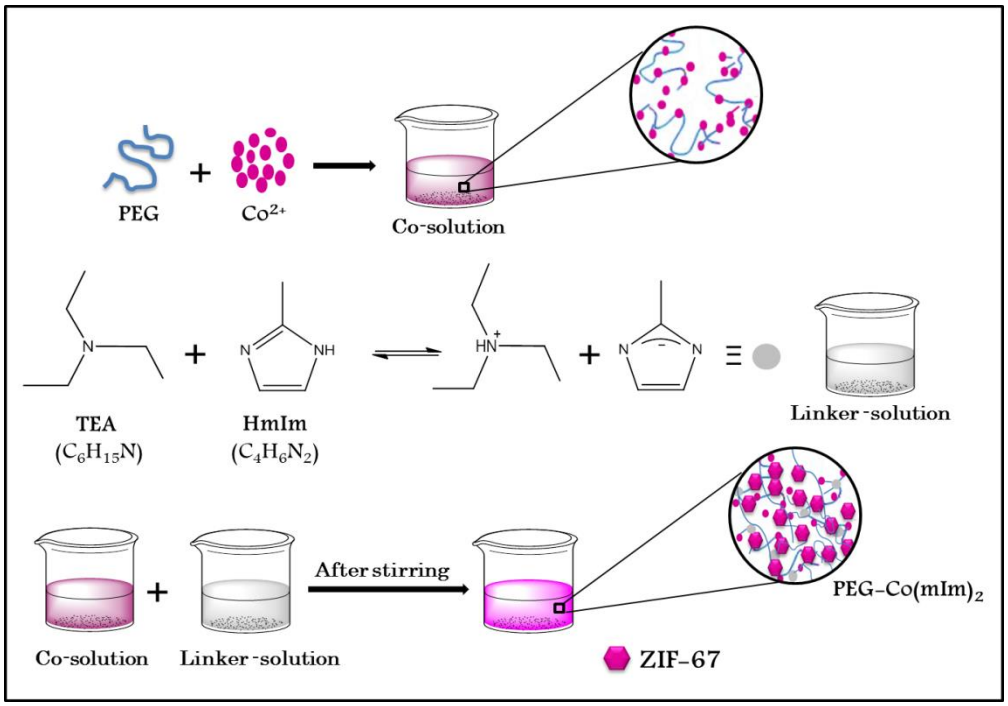

Scheme 1: Room temperature synthesis reaction to obtain PEG-template ZIF-67 (n-ZIF-67).

Table 1. Comparison of the CO_2 and CH_4 adsorption parameters diverse MOFs and ZIFs

ZIFs/ MOFs	Soft template	BET surface area m^2/g	Particle Size (nm)	Pore volume cm^3/g	Pore diameter (nm)	CO_2 adsorption (mg/g)	CH_4 adsorption (mg/g)	CO_2/CH_4 Selectivity	Ref
Zr-MOF[a]	none	1433	63	0.63	0.88	356.1 (273, 9.8 bar)	57.6 (273, 9.8 bar)	2.2-3.6	[12]
HKUST-1[b]	none	1571	-	0.79		558.8 (298 K, 15 bar)	73.6 (298 K, 15 bar)	-	[13]
ZIF-68[c], **69**[a]	none	1090, 950	-	-	1.03, 0.78	61.6-79.2 (298 K, 1bar)	102.4 (298 K, 1 bar)	5.5-5.6	[14]
Mg-MOF-74[e]	none	1174	5000-25000	0.648	1.02	360.8 (298 K, 1 bar)	16.0 (298 K, 1 bar)	-	[15]
MIL-120[f]	none	-	-	-	-	211.8 (303 K, 10 bar)	28.8 (303 K, 10 bar)	-	[16]
ZIF-93[g]	none	864	-	0.46	1.79	407 (298 K, 60 bar)	-	-	[17]
ZIF-11[h]	none	-	-	0.46	1.49	269.3 (298 K, 40 bar)	-	-	[17]
ZIF-7[i]	none	-	-	0.21	0.75	89.8 (298 K, 40 bar)	-	-	[17]
ZIF-71[j]	none	1025	1000-2000	-	1.65	356.4 (298 K, 45 bar)	-	-	[18]
ZIF-8[j]	PDADMAC[k]	1264	57	0.51	-	347.6(298 K, 40 bar)	-	-	[19]
ZIF-8	none	1475		0.70	-	36.1(298 K, 1 bar)	-	-	[20]
ZIF-8	none	1502	90	0.54	0.7-1.2	469.9 (298 K, 40 bar)	-	-	[21]
ZIF-67[l]	none	1478	500-1000	0.66	0.64-1.04	513.9 (298 K, 50 bar)	-	-	[22]
n-ZIF-8	PEG[m]	1694	150	0.67	0.787	51.5 (298 K, 1 bar)	36.0 (298 K, 1 bar)		
n-ZIF-8	PEG	1694	150	0.67	0.787	547.0 (298 K, 40 bar)	211.58 (298 K, 40 bar)	3.00-8.06	[23]
n-ZIF-67	PEG	1891	66	0.86	0.64	72.0 (298 K, 1bar)	49.0 (298 K, 1 bar)		This
n-ZIF-67	PEG	1891	66	0.86	0.64	681 (298 K, 40 bar)	241 (298 K, 40 bar)	3.67-16.05	work

[a]$Zr_6O_4(OH)_4(BDC)_6$ with BDC: 1,4-dicarboxybenzene; [b]$Cu_3(BTC)_2$ with BTC: benzene-1,3,5-tricarboxylic acid; [c]Zn(bIm)(nIm) with bIm: benzimidazole and nIm: 2-Nitroimidazole; [d]Zn(cbIm)(nIm) with cbIM: 5-chlorobenzimidazole; [e]$Zn_2(dhtp)(H_2O)_2.8H_2O$ with dhtp: 2,5-dihydroxyterephthalate; [f]$Al_4(OH)_8(BTEC)$ with BTEC: 1,2 ,4,5-benzenetetracarboxylic acid ; [g]$Zn(almeIm)_2$ with almeIm: 4-methylimidazole-5-carbaldehyde; [h]$Zn(bIm)_2$ with bIm: benzimidazole; [i]$Zn(bIm)_2$; [j]$Zn(dcIm)_2$ with dcIm: 4,5-dichloroimidazole; [j]$Zn(mIm)_2$ with mIm: 2-methylimidazolate; [k]PDADMAC: poly(diallyldimethylammonium chloride) ; [l]$Co(mIm)_2$; [m]PEG as polyethylene glycol (average molecular weight = 20.000 g mol^{-1})

2.3. Characterization

FTIR spectroscopy was performed using a Perkin Elmer Spectrum Two instrument with attenuated total reflectance (ATR) spectra recorded from 4000 to 400 cm^{-1}. X-ray powder diffraction spectra (XRD) from 5° to 60° were recorded on a Bruker D8 Discover diffractometer with a scanning rate of 2°/min. The morphology and elemental composition of n-ZIF-67 was determined by transmission electron microscopy (TEM, Philips CM200) combined with an energy-dispersive X-ray spectrometer (EDX). The particle size analyses were determined using Image J software. Thermogravimetric analysis curves (TGA) were measured on a Mettler Toledo STARe apparatus by heating the samples from 298 K up to 973 K at a heating rate of 2°C/min under an air atmosphere. At 77 K, nitrogen adsorption-desorption isotherms (Micrometrics ASAP-2420 instrument; sample degassing at 423 K for 24 h under vacuum) were collected to determine the Brunauer-Emmett-Teller (BET) specific surface area (P/P° ranging from 0.01 to 0.35), total micropore volume (V_P), and pore size distribution (t-plot method).

2.3 CO_2, CH_4, and N_2 adsorption

Pure component adsorption isotherms of CO_2, CH_4, and N_2 at n-ZIF-67 and n-ZIF-8 were obtained by gravimetric analysis (Autosorb-iQ-MP analyzer) in the range of 0-40 bar at different temperatures: 273, 298, 323 and 353 K. The samples were degassed at 423 K under a high vacuum for 24 hours prior to the sorption measurement. The CO_2 used was of high purity (99.99%) and obtained from Sigma-Aldrich. The gases used wereall high purity (99.99%) and obtained from Sigma-Aldrich. Numerous adsorption kinetic models were employedto define the adsorption equilibrium isotherm data. In this work, the Langmuir adsorption kinetics model (Eq. (1)) was used to fit the equilibrium isotherm data [32]. This model was used to describe the monolayer pattern of the adsorbed layer on the homogeneous surface. The Langmuir equation can be expressed by the equilibrium adsorption capacity (q, mg/g), maximum adsorption capacity (q_m, mg/g), Langmuir isotherm constant or a parameter related to the affinity constant between adsorbate and adsorbent (K_L, L/g), and partial pressure (P, bar)as Eq. (1).

$$q = q_m \frac{k_L P}{1 + k_L P} \qquad \text{Eq. (1)}$$

3. Results and discussion

3.1 Structural analysis

The FTIR spectrum of the PEG templated n-ZIF-67 recorded between 400 and 4000 cm^{-1} is shown in Fig. 1. The n-ZIF-67 structure contains the ligand, mIm, which is responsible for most of the band characteristics. Precisely, the bands that appeared between 600 and 1500 cm^{-1} are ascribed to bending and stretching of the imidazole ring, such as the bands at 1145 and 1308 cm^{-1}, for the bending signal, and bands at 1415 and 1433 cm^{-1}, for the stretching vibrations [31, 33]. The bands at 994 and 750 cm^{-1} can be attributed to the bending vibrations of C–N and C–H, respectively, while the band at 694 cm^{-1} can be attributed to the bending variation of the mIm ring. The absorption band at 1637 cm^{-1} is due to the C=C stretch mode, whereas the absorption band at 1584 cm^{-1} is attributed to the stretching mode of C=N. The two small absorption bands at 2929 and 3136 cm^{-1} can be accredited to the asymmetric stretching modes of the aliphatic C–H and the aromatic ring of mIm, respectively. Interestingly, the

Co=N stretching vibration band is observed at 424 cm^{-1} [34], suggesting that the cobalt ions are linked chemically with nitrogen atoms of the methylimidazole (mIm) groups to shape the imidazolate. The FTIR results confirmed the successful synthesis of pure ZIF-67 [35].

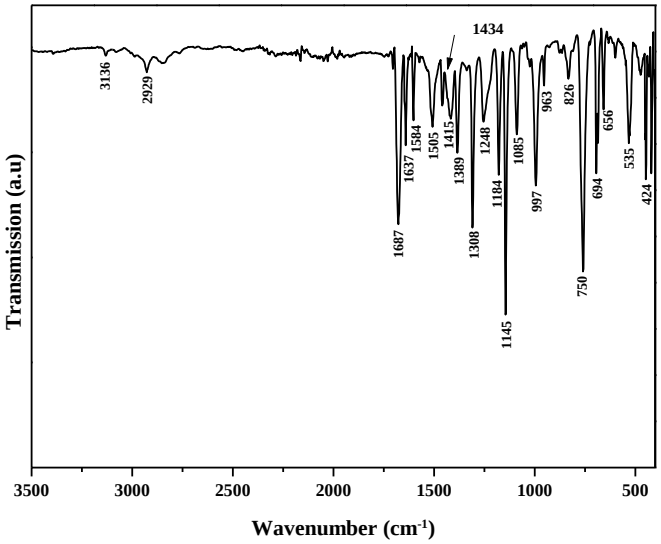

Fig.1. FTIR spectrum of n-ZIF-67.

As was mentioned in Section 2.2, n-ZIF-67 NPs were rapidly synthesized in minutes. The material was isolated in about 1 hr with the synthesis process occurring at room temperature and pressure. The method is rapid but also easily scalable, although with the notable downside that DMF and methanol solvents are used. The X- ray powder diffraction method was used for analyzing the chemical composition of as-produced n-ZIF-67 NPs. The sharp diffraction peaks at 2θ values of 7.4°, 10.4°, 12.8°, 14.7°, 16.5°, 18.0° and 19.5°, 22.1°, 24.5°, 26.7°, and 29.6° are assigned to the ZIF-67 planes of (011), (002), (112), (022), (013), (222), (114), (233), (134) and (044), respectively [36]. The XRD diffraction pattern with Rietveld refinement in Fig. 2 represents the common peaks of ZIF-67 and matches well with the simulated ZIF-67 diffractogram [36, 37]. Crystallite sizes were calculated using the Debye-Sherrer equation (Eq. 2) [38- 40]:

$$L = \frac{K\lambda}{\beta\cos\theta} \qquad \text{Eq. (2)}$$

Where L is the diameter of the crystallites (nm), K is the numerical Scherrer constant (0.93 Å), λ is the X-ray wavelength (1.54 Å), β is the full width at half-maximum intensity (FWHM) in radians, and θ is the Bragg diffraction angle. The crystallite size of n-ZIF-67 NPs was first determined using the Debye-Scherrer equation, equal to about 78 nm. The refined XRD structural parameters, calculated grain sizes, crystallite sizes and strains of n-ZIF-67 are collated in Table 2.

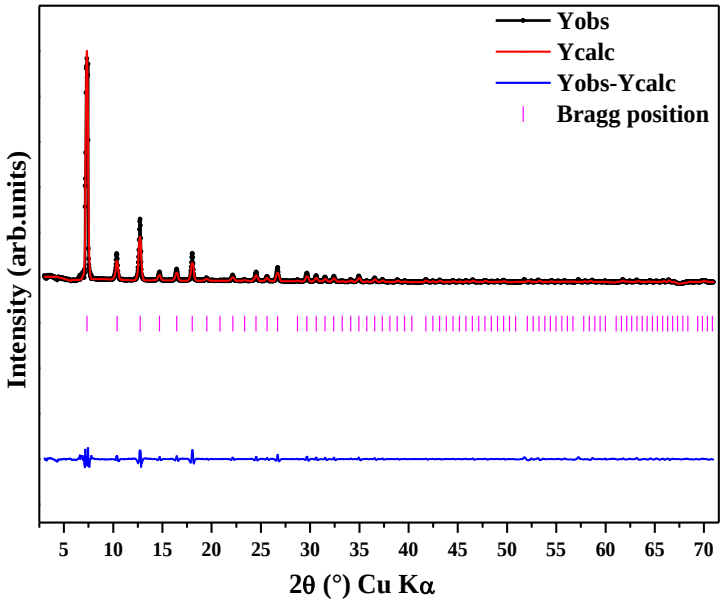

Fig.2: Rietveld plots of the XRD data for the PEG templated n-ZIF-67 ($Co(mIm)_2$ with the observed (black line), calculated (solid line), calculated Bragg reflection positions (vertical purple line), and the difference pattern between observed and calculated profiles (blue line, bottom).

Next, we considered the Williamson-Hall (W-H) method to determine the size for comparison with the Scherrer technique and TEM data. In the W-H method [41], the strain induced broadening arising from crystal imperfection and distortions is related by: $\beta_s = 4\varepsilon \tan(\theta)$ Eq. (3)

Here, ε is the root mean square value of the micro-strain, $\varepsilon = \frac{\Delta d}{d}$. Assuming that the particle size and strain contributions to line broadening are independent of each other and that both have a Cauchy like profile, the observed line breadth is simply the sum of the two: $\beta_{hkl} \cos(\theta) = \frac{k\lambda}{D} + 4\varepsilon \sin(\theta)$ Eq. (4)

A plot is drawn with $\sin(\theta)$ along the x-axis and $\beta_{hkl} \cos(\theta)$ along the y-axis for as-prepared PEG-templated n-ZIF-67 (Fig 3 (a)). The slope and y-intersect of the fitted line represent the strain and the particle size respectively. We can remark that the calculated crystallite size using the W-H technique (D_{W-H} = 91 nm) is larger than that calculated using Scherrer's technique (78 nm). This is due to the presence of strain which also contributes to the broadening of peaks. The grain sizes observed by TEM (see Fig. 3 and discussion below) are larger than those calculated by Scherrer's and W-H techniques. This can be explained by the fact that each particle observed by TEM is formed by several crystallized grains.

Table 2: Refined structural parameters and calculated grain sizes, crystallite sizes and strains of n-ZIF-67

n-ZIF-67 [Co (mIm)$_2$]	Cubic
Space group	I -4 3 m
Cell parameters	a=b=c = 17.0545 (1) Å
Cell volume	4873.139 (2) Å^3
Discrepancy factors (%)	R_p = 0.339 R_F = 0.914 R_{wp} = 0.53 χ^2 = 1.94
Bragg R factor	1.34
D_{TEM} (nm)	~ 30 - 100
D_{sch} (nm)	78
$D_{W\text{-}H}$ (nm)	~ 91
Strain (ε)	0.000325

The morphology of n-ZIF-67 was studied using TEM. According to Fig. 3 (b), the uniform rhombic dodecahedralmorphology was observed for ZIF-67 NPs, in agreement with a previous study of ZIF-67 nanocrystals [42]. The perfect crystalline structure of the synthesized n-ZIF-67 NPs was further confirmed by the well-defined rhombic facet and the clearly visible edge of ZIF-67. In addition, the surfaces of the particles appear regular and smooth, and the particles do not appear to be aggregated. Further interpretation of the TEM images using ImageJ software revealed that the particles had a Gaussian distribution, ranging from 30 to 100 nm, (Fig. 3 (c)), close to the size of the crystallites indicated via the Williamson-Hall data and the Debye-Scherrer equation (about 78 nm). The EDX analysis data, as shown in Fig. 3 (d), clearly demonstrates the expected elemental characteristic peaks for C (0.26 keV), N (0.53 keV), and Co (1, 6.9 keV), confirming the successful synthesis of ZIF-67 NPs.

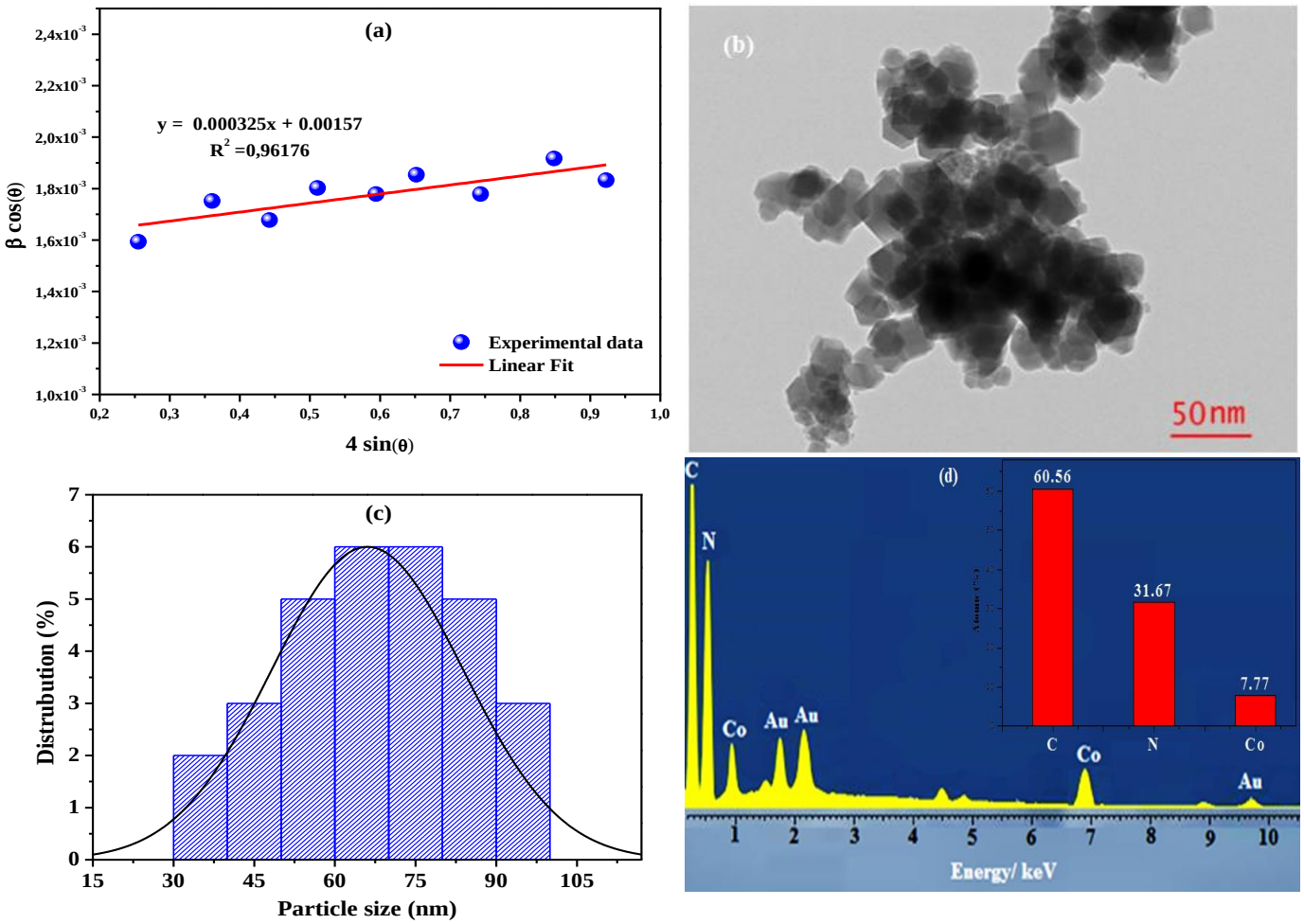

Fig.3. (a) strain graph of the cubic phase of n-ZIF-67 NPs (b) TEM image (c) TEM-based particle size distribution and (d) EDX spectrum

3.2. Thermal analysis

Thermal stability analysis of n-ZIF-67 NPs was conducted based on TGA curves. Fig. 4 depicts the weight loss rate and weight loss profiles. It is evident that a two-stage weight loss occurred at n-ZIF-8. The first weight loss was detected between 300 and 680 K, related to the removal of physisorbed molecules (e.g. H_2O, CO_2, and methanol) from the framework, concomitant with several exothermic peaks. The second weight loss at 700 K is followed by a rapid loss and exothermic peaks, which can be associated with the decomposition of the ZIF-67 NPs. The high thermal stability of ZIF-67 NPs, based on TGA curves, is consistent with previously reported data [34, 43, 44]. It was found that about 12 wt% of the initial weight of the powder remained after decomposition, which can be attributed to cobalt oxide, CoO, formation.

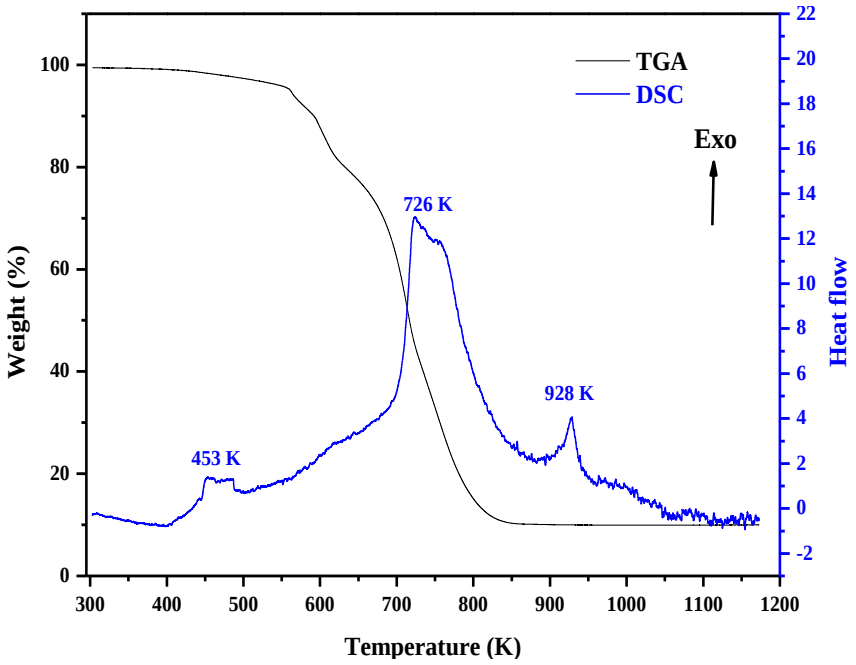

Fig.4. Thermal stability analysis of PEG-templated n-ZIF-67 (heating rate of 2°C/min; in air).

3.3. Nitrogen isotherm and pore size distribution

Considering the TGA analysis data in Section 3.2, n-ZIF-67 NPs were degassed at 423 K prior to N_2 isotherm measurements. Fig. 5 displays the pore size distributions and N_2 adsorption isotherms for n-ZIF-67. As shownin Fig. 5 (a), the adsorbent showed a N_2 rapid uptake at a the very low relative pressure region ($10^{-5} < P/P° < 10^{-2}$). Based on the IUPAC classification, the sample had a typical type I isotherm [23, 35, 45] that confirms the microporosity of the material. As shown in Fig. 5, n-ZIF-67 NPs had reversible and reproducible N_2 adsorption and desorption isotherms, emphasising a stable material with permanent porosity and good rigidity. The BET method was employed to measure the sample porosity at $0.001 < P/P_0 < 0.35$. The BET surface area (S_{BET}) of the PEG-templated n-ZIF-67 NPs was 1871 m^2/g with a micropore volume of 0.86 cm^3/g, which are higher than previous values reported for ZIF-8 (including PEG-templated ZIF-8) and ZIF-67, as summarized in Table 1, highlighting the attractive adsorption potential of the new material reported here [23, 24]. The total pore volume (V_{micro}) of n-ZIF-67 was 0.86 cm^3/g at P/P° = 0.99. Fig. 5 (b) illustrates that the predominant pores of the MOF are 0.64 nm in diameter (ultramicropores). Such ultramicropores are expected to favor the adsorption of CO_2 molecules and eventually their preferential adsorption compared to N_2 and CH_4 molecules, based on geometric considerations (CH_4 (0.38 nm) > N_2 (0.364 nm) > CO_2 (0.33 nm)) [46].

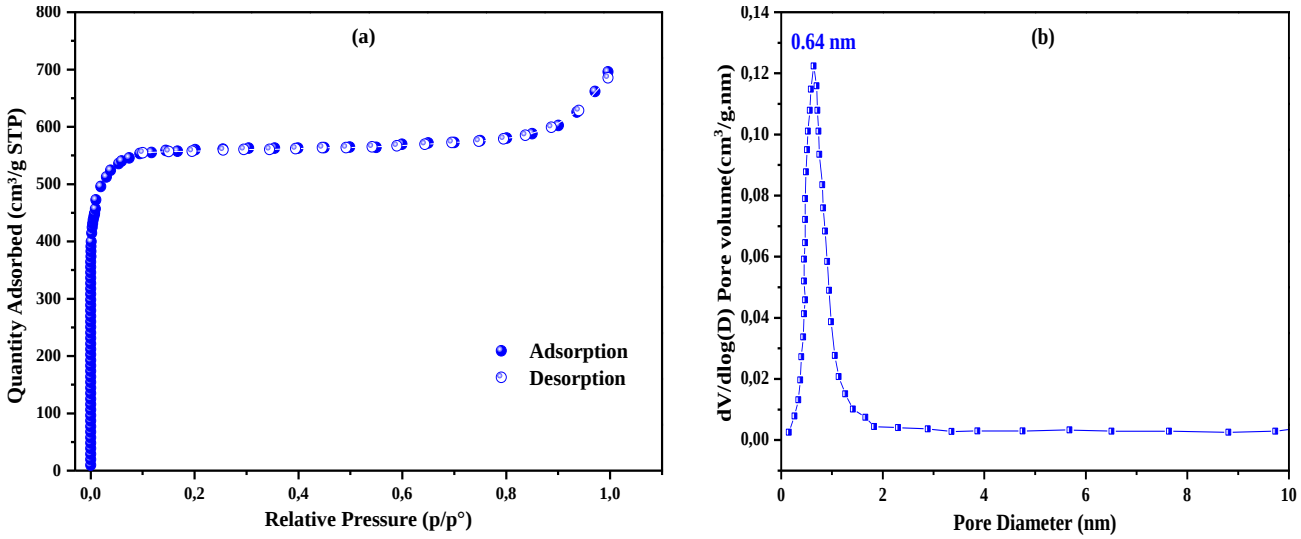

Fig. 5. (a) N_2 adsorption-desorption isotherms for n-ZIF-67, and (b) the corresponding pore sizedistribution.

3.4. CO_2, CH_4 and N_2 adsorption

The CO_2, CH_4, and N_2 adsorption isotherm performance at n-ZIF-67 and n-ZIF-8, with Langmuir adsorption model fitting, was subsequently investigated at low pressure (0 to 100 KPa/0 to 1 bar) and high pressure (0 to 40,000 KPa/0 to 40 bar) at different temperatures (273, 298, 323, and 253 K) after outgassing at 423 K. Nanoscale ZIF-67, due to its excellent textural properties including large porosity (microporosity and ultramicroporosity) and crystallinity, is an attractive candidate for the adsorption of gases such as CO_2, CH_4 and N_2, and especially the electrophile, CO_2, via interactions with its active adsorption sites within its pores [47, 23]. The high selectivity of ZIFs for CO_2 in gas mixtures, especially industrially important CO_2/N_2 and CO_2/CH_4 mixtures, is an attractive point that we endeavored to explore with PEG-templated n-ZIF-67. At low-pressure, between 0 and 100 KPa) and at different temperatures between 273 and 353 K, the CO_2 uptake of PEG-templated n-ZIF-67 increased quasi-linearly with increasing pressure (Fig. 5 (a)). At 100 KPa CO_2, the uptake did not reach saturation. According to the IUPAC classification, CO_2 and CH_4 exhibited a non-linear type I isotherm, which is in contrast to the N_2 isotherms which showed a linear adsorption behavior (Fig. 5 (a, c, and e)). In contrast, at PEG-templated n-ZIF-8, all of the gas adsorption isotherms exhibited a linear adsorption behavior (Fig. 5 (b, d, and f). The n-ZIF-67 particles showed a higher adsorption capacity for all gases at 100 KPa compared to n-ZIF-8. At 298 K and 100 KPa, the adsorption capacity of CO_2 at n-ZIF-67 was 111.89 mg (CO_2)/g, which was higher than the 51.5 mg(CO_2)/g recorded at PEG-templated n-ZIF-8 samples and ZIF-8 (Table 1) [20, 23]. The higher CO_2 capture capacity observed for n-ZIF-67 can be attributed, at least in part, to the combination of a higher BET surface area (1871 m^2/g) and pore volume (0.86 cm^3/g), and the ultramicropores below 0.7 nm (0.64 nm). Linked to the physical interactions of the free pore sites of ZIF-67 with CO_2 molecules, [49, 23], n-ZIF-67 adsorbed more CO_2 at 273 K (850.52 mg(CO_2)/g) than at higher temperatures such as 353 K (425.04 mg (CO_2)/g. An analogous behaviour has been observed and defined previously for ZIF-8, ZIF-69, and ZIF-76 [23, 49]. Additionally, the n-ZIF-67 material prepared here showed maximum adsorption capacities for CH_4 and N_2 of 40.72 mg(CH_4)/g for CH_4 and 23.02 mg(N_2)/g for N_2 at 298 K and 100 KPa (see Table 1). These adsorption capacities surpassour previous results with PEG-templated n-ZIF-8. This higher adsorption capacity for all three gases compared to n-ZIF-8 highlights the very promising physical characteristics of the newly synthesized n-ZIF-67 material.

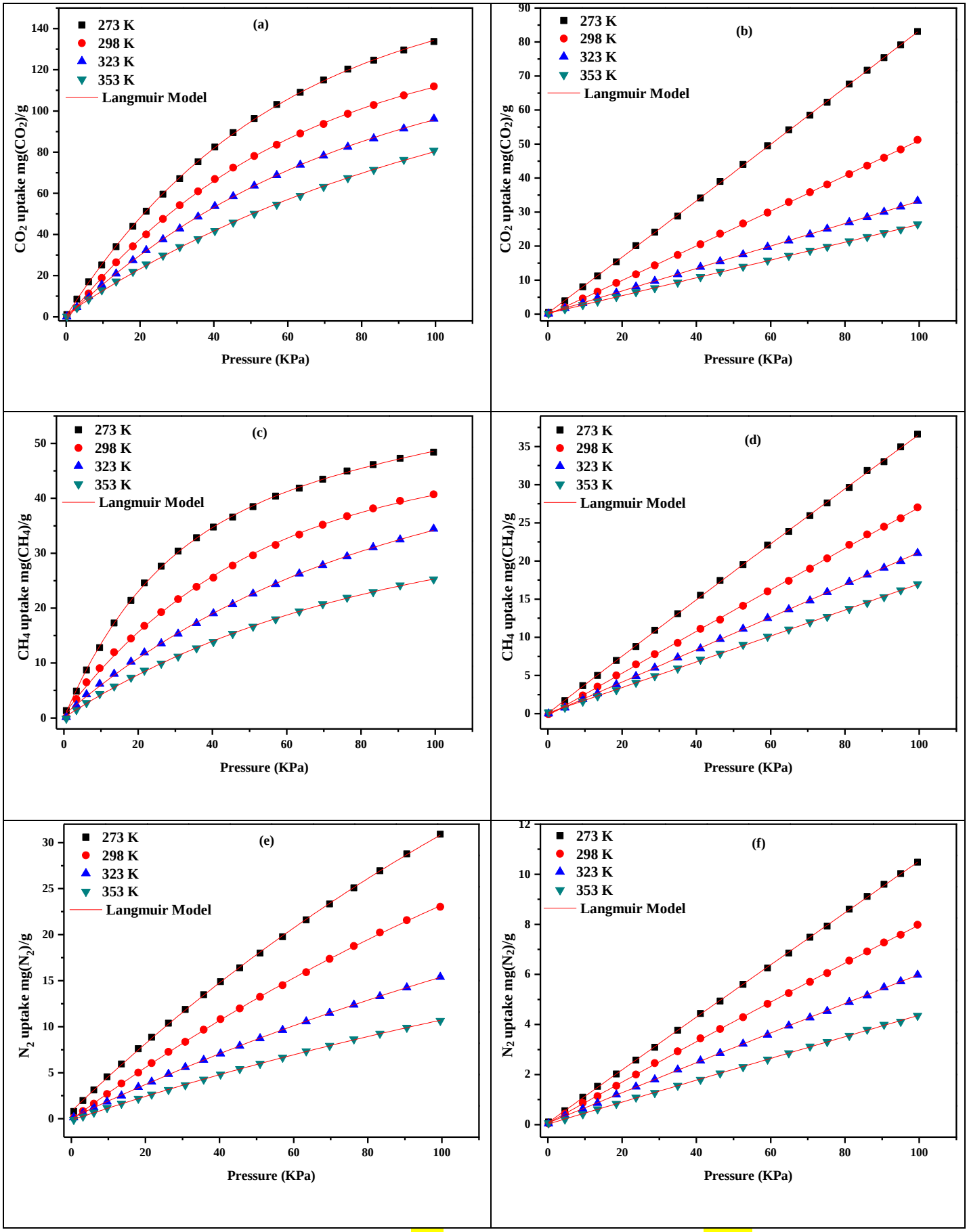

Fig. 6. CO_2, CH_4, and N_2 adsorption isotherms with Langmuir adsorption kinetic model fitting of n-ZIF-67 (a, c, e) versus n-ZIF-8 (b, d, f) at different temperatures (273, 298, 323, and 353K) and low pressure (0-1 bar)

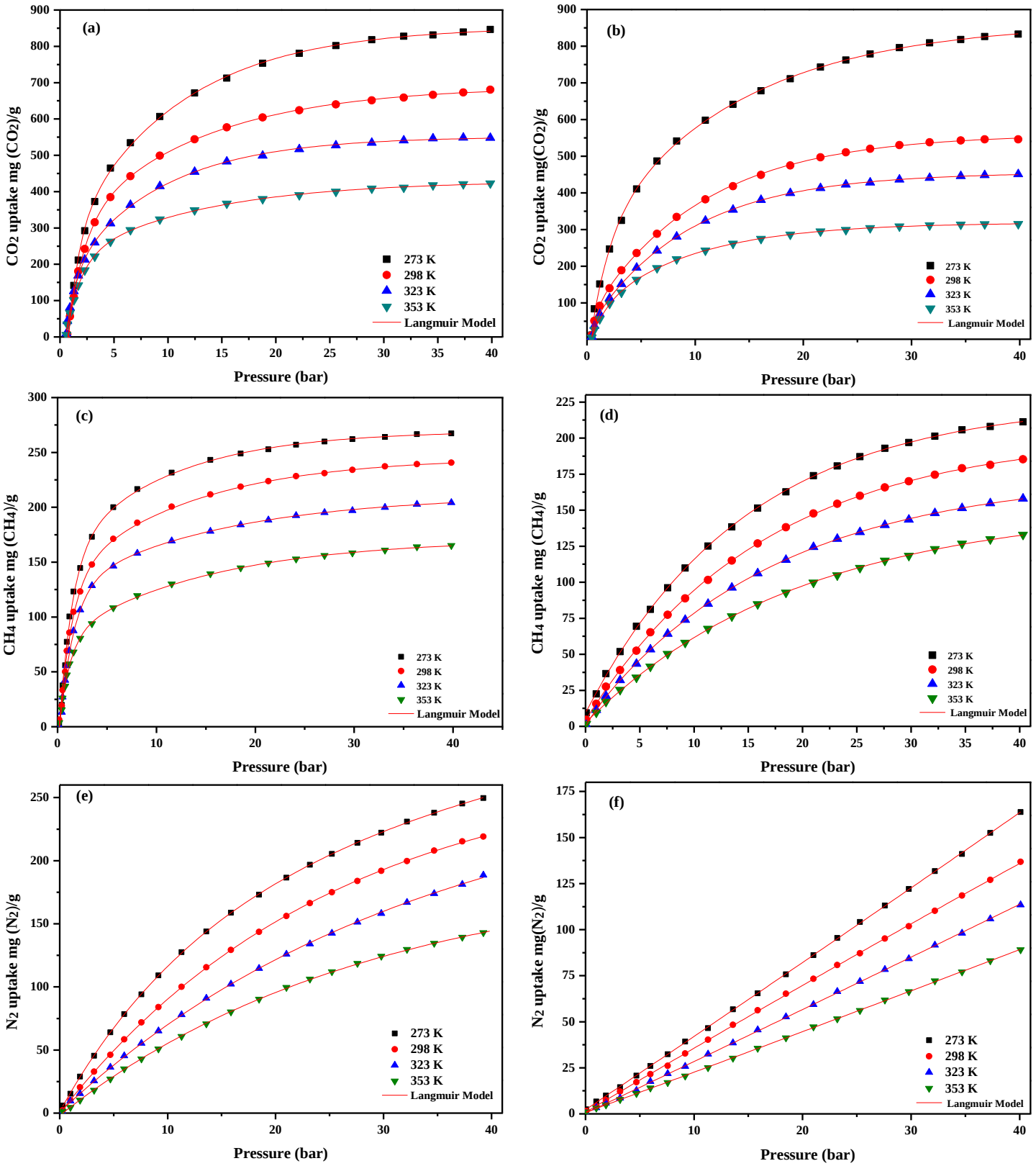

Fig. 7. CO_2, CH_4, and N_2 adsorption isotherms with Langmuir adsorption kinetic model fitting of n-ZIF-67 (a, c, e) with versus n-ZIF-8 (b, d, f) at different temperatures (273, 298, 323, and 353K) and high pressure (0-40 bar).

The adsorption isotherms of CO_2, CH_4, and N_2 at both n-ZIF-67 and n-ZIF-8 at various temperatures (273, 298, 323, and 353 K) and high pressure (0-40 bar) were also considered (Fig. 7). Generally, CO_2 and CH_4 adsorption increases with elevated pressure and the uptake reaches saturation at both materials. The N_2 uptake increases linearly with increasing pressure. The n-ZIF-67 samples showed significantly higher CO_2 adsorption capacity compared to CH_4 and N_2 adsorption, and higher adsorption capacities for all gases compared to n-ZIF-8 [23]. The adsorption capacity of 681 mg (CO_2)/g at n-ZIF-67 at 298 K and 40 bar CO_2 is the maximum capacity reported for a ZIF-67 and ZIF-8 adsorbent, as far as the authors are concerned (Table 1). The highest adsorption capacity achieved in this study was 846 mg (CO_2)/g at 40 bar for n-ZIF-67. This exceptional adsorption capacity at higher pressures further underlines the beneficial physical properties linked to the very large BET surface area and the ultramicropores of the n-ZIF-67 structure. Under the same conditions of 298 K and 40 bar, the adsorption capacities for CH_4 on n-ZIF-67 and n-ZIF-8 were 241 and 211.58 mg(CH_4)/g, respectively, while the N_2 adsorption capacities were 219 and 137 mg(N_2)/g, respectively. It is noted that at higher pressures, the N_2 isotherms revealed a quasi-linear behavior while the CO2 and CH4 isotherms showed type I behavior.

As discussed prior, according to the adsorption isotherms in Fig. 7, both n-ZIF-67 and n-ZIF-8 adsorbents had higher adsorption capacities for CO_2 compared to CH_4 and N_2. In addition to the smaller size of the molecule that corresponds well with the sub 1 nm micropores and especially the 0.64 nm ultramicropores of n-ZIF-67, CO_2 has an important quadrupole moment (13.4×10^{-40} C.m^2) compared to N_2 (4.7×10^{-40} C.m^2). These factors combined are consistent with better interactions via physisorption of CO2 at the surface of these zeolitic imidazolate frameworks MOFs, and especially n-ZIF-67 [50, 51]. The presence of a large quadruple moment in the CO_2 molecule can facilitate interactions with the electric field gradient inside pores as well as eventually short-range dipole-quadrupolar interactions. CH_4 on the other hand does not have a dipole or quadrupole moment but it does have a weak electric octuplet moment that could play a role in the adsorption of this gas [52].

Another factor to consider is that the three gases possess different electronic properties and therefore polarizabilities The greater polarizability of CH_4 molecules: 17.6×10^{-25} vs. 26.0×10^{-25} cm^3 for N_2 and CH_4, respectively can help to explain the better adsorption capacity of CH_4 compared to N_2 [53].

The adsorption isotherms of CO_2, CH_4, and N_2 for n-ZIF-67 and n-ZIF-8 fitted well to the Langmuir adsorption kinetics model (Eq. (1)). Table 3 shows the equation parameters used and the highly correlated correlation coefficient values for the data fitting according to the Langmuir model for n-ZIF-67. The maximum CO_2 adsorption capacity (q_m) according to the Langmuir adsorption model approach was also higher for n-ZIF-67 compared to n-ZIF-8 (Table 3). The value of the correlation coefficient highlights the slightly more homogeneous nature of the n-ZIF-67 adsorbent surface compared to ZIF-8 where values of R^2=0.996 were reported [23]. According to the Langmuir isotherm kinetic model, the q_m and K_L decreased at higher temperature, suggesting an exothermic adsorption process [23, 54].

Table 3 Equation parameters for the Langmuir isotherm model for PEG-templated n-ZIF-67

Adsorbate	T(K)	$Q_{m\ (mg.g^{-1})}$	$k_{L\ (L.\ g^{-1})}$	R^2
CO_2	273	854.48	1.98	0.998
	298	690.39	1.75	0.999
	323	551.40	1.62	0.999
	353	429.83	1.48	0.998
CH_4	273	269.67	1.46	0.999
	298	245.71	1.38	0.999
	323	211.02	1.29	0.999
	353	171.22	1.14	0.999
N_2	273	259.12	1.22	0.999
	298	229.32	1.16	0.999
	323	188.51	1.09	0.999
	353	142.98	0.98	0.999

The important characteristics of the Langmuir isotherm, the separation factor (R_L), can be represented by Eq. 5 [55].

$$R_L = \frac{1}{1+k_L P} \qquad \text{Eq. (5)}$$

Where K_L is the Langmuir constant and P (bar) is the pressure. For $R_L = 0$ (K_L is very large), irreversible adsorption; for $R_L = 1$ ($K_L = 0$), linear adsorption; for $0 < R_L < 1$, favorable and $R_L < 1$ ($K_L < 0$), unfavorable adsorption (that is, desorption). The values of R_L for all gases were determined over a wide pressure range and the results are shown in Fig. 8. All the R_L values are between 0 and 1, indicating that all three gases (CO_2, CH_4, N_2) are favorably adsorbed at n-ZIF-67 in the studied pressure range from 0 to 40 bar.

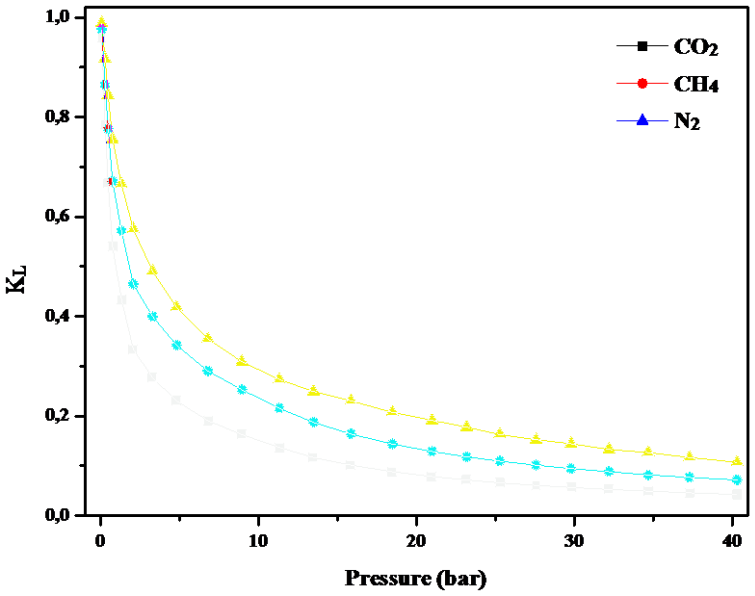

Fig. 8. Separation factor (R_L) plot against pressure for gas adsorption at n-ZIF-67.

3.5. Isosteric Heat of Adsorption

The isosteric heat of adsorption (Q_{st}) is an important parameter in gas adsorption studies. It allows us to understand how the adsorbent and adsorbate interact. According to the Langmuir kinetic model, the adsorption enthalpy of CO_2 at PEG-templated n-ZIF-67 was estimated from the experimental adsorption isotherms determined at different temperatures. From the Langmuir fitting parameters (Table 3), the adsorption enthalpy was calculated, following

the Clausius-Clapeyron equation (Eq. (6)) [56]

$$Qst = -RT^2 \left(\frac{d\ln(P)}{dT}\right) \qquad \text{Eq. (6)}$$

In which: T (K) is the temperature; P is the pressure (bar); R (8.314 J mol^{-1} K^{-1}) is the universal gas constant and Q_{st} is the heat of adsorption in KJ/mol. Based on the general hypothesis that the enthalpy of adsorption is independent of the temperature, the combination of equation 6 offers:

$$\ln P = \left(\frac{Qst}{RT}\right) + C \qquad \text{Eq. (7)}$$

In which: C is the constant.

In this study, the heat/enthalpy of adsorption (Q_{st}) of CO_2, CH_4, and N_2 were determined by linear plotting of the logarithm of the pressure (ln (P)) versus the reverse of the temperature (1/T) by using the equilibrium isotherm data. Fig. 9 (a) shows the heat of adsorption for all gases at zero loading for both n-ZIF-67 and n-ZIF8 frameworks Fig. 9 (b) shows Q_{st} as a function of the CO_2 uptake. The Q_{st} value is associated with different forces depending on the nature of the interaction between adsorbent-adsorbate, such as Van der Waals forces, dipole-dipole and dipole-quadrupole interactions, and chemical bonds.

According to the work of Zhou et al. [57], the Q_{st} value for physisorption is lower than 80 KJ/mol, while, it is between 80 and 200 kJ/mol for chemisorption. The heat of adsorption at zero loading for both samples, n-ZIF-67 and n-ZIF-8, are presented in Fig .9 (a). For the studied gases, the heats of adsorption were higher at n-ZIF-67 compared to n-ZIF-8. This corresponds well with a stronger interaction between the adsorbates and the ultramicropores in n-ZIF-67 framework. The largest relative increase in Qst between the two types of ZIF structures was observed for CO_2. The CO_2 gas, with its quadrupole moment, is considered especially strongly interacting with the ultramicropores in n-ZIF-67. For n-ZIF-67 and n-ZIF-8, the heats of adsorption at zero loading of CO_2 were 34.44 KJ/mol and 27.60 KJ/mol, respectively. The Q_{st} values attained for both adsorbents were less than 80 KJ/mol, indicating that the gas adsorption processes were controlled by physical rather than chemical adsorption.

Fig. 9 (b) shows the variation of the heat of adsorption values at 298 K for CO_2, CH_4, and N_2 at ~~on~~ n-ZIF-67. At low adsorption pressure, the heat of adsorption of CO_2 was greater than for either CH_4 or N_2. With an increase in adsorption uptake, the heat of CO_2 adsorption was reduced, owing to a decrease in the number of active adsorption sites as a result of the firm interaction of CO_2 with the ultramicroporous structure for n-ZIF-67, the enthalpy of adsorption for CO_2 was 34.44 KJ/mol at zero loading and 29.19 KJ/mol at high loading. Consequently, the enthalpy of adsorption of CO_2 decreases when the CO_2 adsorption capacity increases; this behavior is linked to the surface heterogeneity of the MOF [23]. In the low pressure region, the CO_2 gas also showed the highest heat of adsorption, thanks in part to its quadrupole moment. CO_2 demonstrated negligible variation in the heat of adsorption with loading, while CH_4 displayed a significant decrease in the heat of adsorption from about 26.51 KJ/mol at zero loading to about 24.99 KJ/mol at a loading of *ca.* 30 mg(CH_4)/g. Furthermore, the heat of adsorption for N_2 at n-ZIF-67 was independent of the N_2 uptake, indicating a weak interaction between N_2 and the n-ZIF-67 material. With regard to the other gases, it is evident that the heat of adsorption of CH_4 and N_2 on n-ZIF-67 was lower than that of CO_2. The data globally confirms the favorable selectivity of the n-ZIF-67 adsorbent for CO_2/CH_4 and CO_2/N_2, respectively.

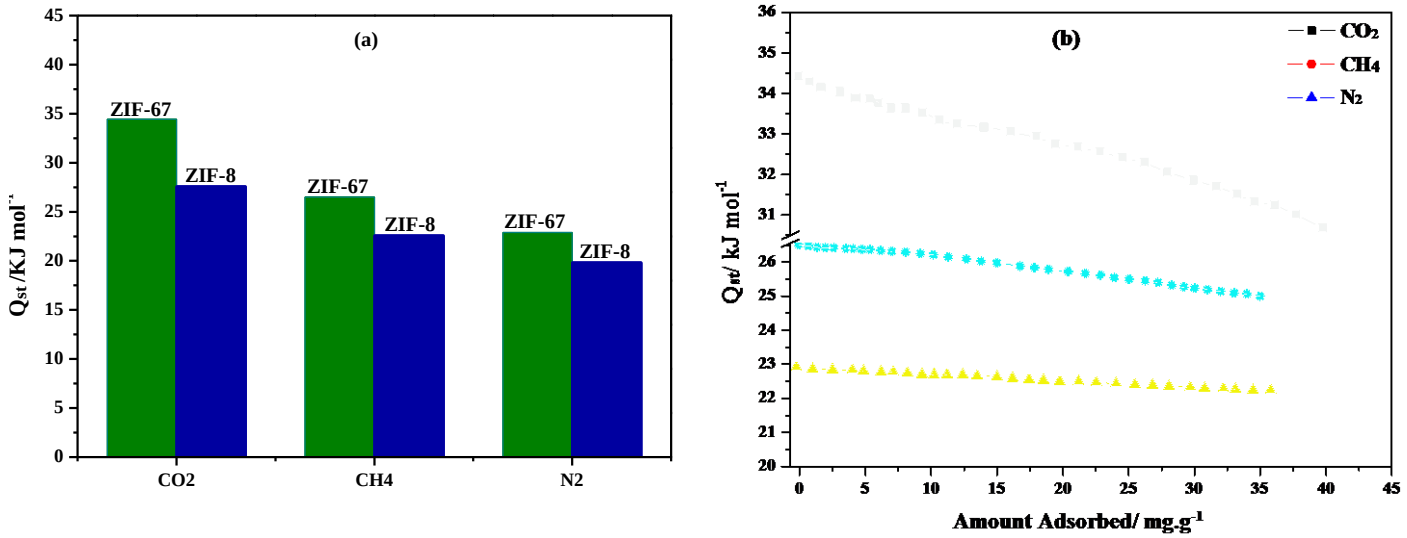

Fig. 9. (a) Comparison of the isosteric heats of adsorption at zero loading at 298 K for CO_2, CH_4 and N_2 at n-ZIF-67 and n-ZIF-8; (b) Variation in the heat of adsorption with loading at n-ZIF-67.

3.6. Selectivity of CO_2/N_2, CH_4/N_2 and CO_2/CH_4 on ZIF-67 NP

The gas selectivity behavior of PEG-templated n-ZIF-8 for CO_2/N_2 CO_2/CH_4 and CH_4/N_2 at n-ZIF-67 was evaluated and is shown in Fig. 10. First we estimated the selectivity by dividing the adsorption capacity of CO_2 by that of N_2 or CH_4 at each pressure point [13, 23, 58]. It is evident from Fig. 10 that ZIF-67's selectivity decreased as the pressure increased for CO_2 over N_2, CO_2 over CH_4, and CH_4 over N_2. Especially in the low-pressure region, the adsorption selectivity for CO_2 from CO_2/N_2 and CO_2/CH_4 mixtures at n-ZIF-67 was consistently higher than that of ZIF-8 materials, as reported in the literature [23, 59]. The n-ZIF-67 selectivity towards CO_2 at 298 K decreased slowly as the pressure was increased. Because of the low heat of adsorption of CO_2 at low pressure, the n-ZIF-67 exhibited lower selectivity towards CO_2 (at 298 K) compared, for example, to zeolite 13X (Q_{st} = 49 KJ/mol) [60]. On the other hand, a lower value is probably beneficial in reducing adsorbent regeneration energy requirements [60]. Furthermore, the CO_2/N_2 selectivity on n-ZIF-67 was maximized in the low-pressure range. As mentioned earlier, CO_2 has a smaller molecular size (3.3 Å), higher polarizability (26.3×10^{-25} cm^3), and a larger quadrupole moment (13.4×10^{-40} $C.m^2$) compared to molecular N_2 (3.8 Å; 17.6×10^{-25} cm^3 and 4.7×10^{-40} $C.m^2$, respectively), that supports the stronger interaction between the active adsorption sites within the ultramicropores of ZIF-67 and the CO_2 adsorbate, which is favorable for CO_2/N_2 separation. Particularly at 0.01, 20, and 40 bar, the CO_2/N_2 selectivity of n-ZIF-67 was up to 28, 11, and 6, respectively, which was higher compared to report ZIF-8 structures [23, 59]. When pressures were low, up to approximately 1 bar, and at 298 K, n-ZIF-67 exhibited a better selectivity for CO_2 over CH_4, with selectivity ranging from 13, at about 1 bar, to 15, at 0.5 bar. The CO_2/N_2 selectivity ranges from 6 to 28, whereas the CO_2/CH_4 selectivity ranges from 4 to 16, which are almost higher than those observed at ZIF-8 [23]. Moreover, with increasing pressure, the selectivity performance decreased. The selectivity for CH_4/N_2 was very low, nearly close to 1. Overall, these selectivity measurements show a high potential for CO_2 separation from CO_2/N_2 or CO_2/CH_4 gas mixtures by gas adsorption at higher pressures.

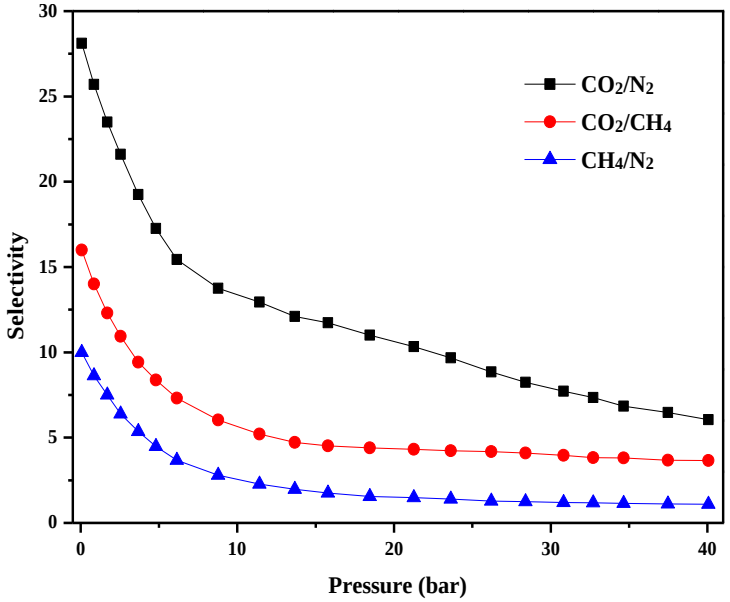

Fig.10. CO_2/N_2, CO_2/CH_4 and CH_4/N_2 selectivity's for n-ZIF-67 at 298 K.

3.7. Breakthrough experiments

In order to confirm the separation performance of PEG-templated n-ZIF-67 for 1:1 ratio CO_2/N_2, CO_2/CH_4 and N_2/CH_4 mixtures, real-time dynamic breakthrough experiments were carried out at 298 K and in the pressure region of 1-10 bar. As shown in Fig. 11 (a,b, c), the breakthrough profiles for the CO_2/N_2 (50/50, v/v) and CO_2/CH_4 (50/50, v/v) mixtures further verify that n-ZIF-67 prefers to adsorb CO_2 over N_2 or CH_4. Importantly, PEG-templated n-ZIF-67 is capable of completely separating CO_2/N_2 (50/50) and CO_2/CH_4 (50:50) mixtures. In addition, it can be seen that N_2 breaks through the fixed n-ZIF-67 adsorbent in a few seconds (Fig. 11 (a), (b) and (c)), revealing a small amount of N_2 is adsorbed. Comparing Fig. 11 (a) with Fig. 11 (b) and (c), we can highlight that the difference in breakthrough time between CO_2 and N_2 is larger than that of the breakthrough time observed between CO_2 and CH_4, and CH_4 and N_2, respectively. It is evident that PEG-templated ZIF-67 has greater CO_2/N_2 selectivity compared to CO_2/CH_4 and CH_4/N_2 selectivity, which is in accordance with the selectivity results obtained in Section 3.6 and Fig.10.

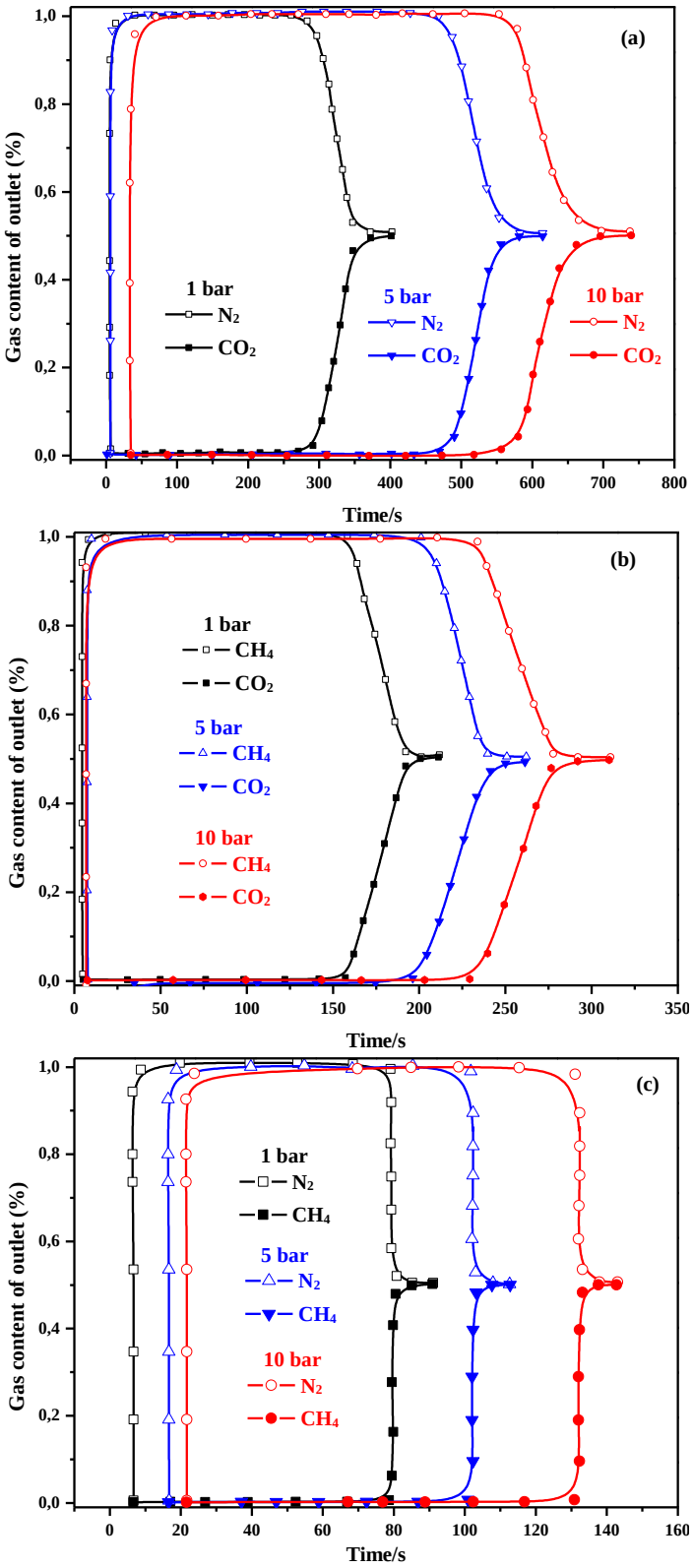

Fig. 11. Breakthrough curves of binary mixtures for (a) CO_2/N_2 (50/50, v/v), (b) CO_2/CH_4 (50/50, v/v), (c) CH_4/N_2 (50/50, v/v) separation experiments with PEG-templated n-ZIF-67 at pressures of 1, 10, 20 bar at 298 K.

3.8. Adsorption/desorption cycles

The adsorption stability of the n-ZIF-67 adsorbent was subsequently evaluated by prolonged cyclic CO_2 and CH_4 adsorption-desorption cycles (15 cycles of adsorption and regeneration). The adsorbents were heated to 423 K (10 K/min) under N_2 gas (50 mL/min) after each adsorption to release any adsorbed gases that remained on the surface of n-ZIF-67. The adsorbent was then cooled to 298 K while being maintained under N_2, and the weight was measured. A subsequent CO_2 adsorption was performed to continue the cycling test. The percentage ratio of the adsorption capacity of the regenerated adsorbent to the fresh one is defined as the adsorption index (AI) and is determined by the equation as follows:

$$AI = \frac{q_n}{q_1} \times 100 \qquad \text{Eq. (8)}$$

Where, q_1 and q_n indicate the CO_2 and CH_4 adsorption capacity of the first cycle and the n^{th} (n = 1-15) cycle, respectively.

The adsorption stability of n-ZIF-67 can be considered as its recyclability. The n-ZIF-67 adsorbent was used/reused over 15 cycles of successive CO_2 adsorption and desorption under the specified condition of 298 K and 40 bar of CO_2 gas (Fig. 12 (a)). It was stated earlier that the CO_2 adsorption capacity of as-prepared n-ZIF-67 was 681 mg (CO_2)/g (100%). In the second cycle, this value dropped to 680.2 mg (CO_2)/g (99.88%). After each cycle, the CO_2 adsorption capacity of n-ZIF-67 was very slightly reduced. The capacity was 679.6 mg (CO_2)/g by the end of the 15^{th} cycle (99.79%). This reduction should be related to the material loss as a result of the recycling process. Nevertheless, the CO_2 adsorption capacity after 15 cycles was still higher than 99%,which confirms the high reusability of the n-ZIF-67 adsorbent. Moreover, the CO_2 adsorption and desorption cycle curves were similar, suggesting the strong stability of n-ZIF-67 and appropriateness of this material for CO_2 adsorption. The extended cyclic CH_4 adsorption on n-ZIF-67 adsorbent was also conducted, and the results are shown in Fig. 12 (b). The results show that the adsorption capacity only decreased from 100% to 99.91% by the end of the 15^{th} cycle, signifying that most CH_4 molecules can also be successfully desorbed throughout the regeneration operation.

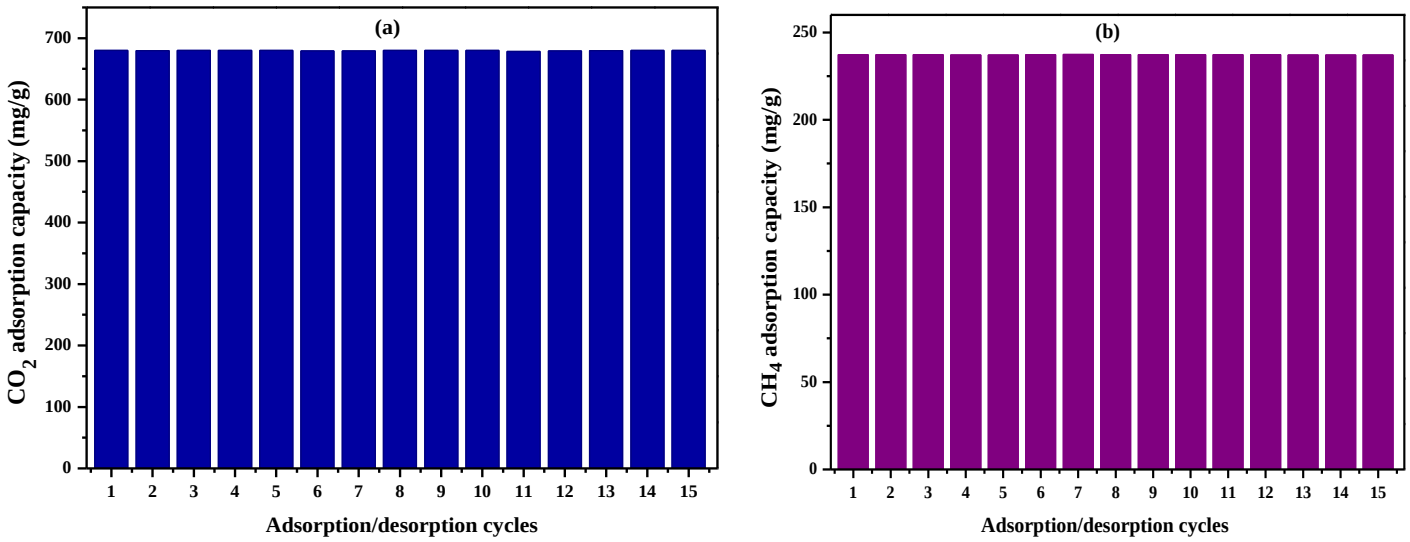

Fig. 12: CO_2 and CH_4 adsorption cycles of ZIF-67 NPs adsorbents.

Conclusion

In summary, PEG-templated hexagonal n-ZIF-67 nanoparticles were successfully synthesized for the first time via a simple and rapid protocol at room temperature. The adsorbent benefits from a very high BET surface of 1891 m^2/g, a large pore volume of 0.86 cm^3/g, and an average ultramicropore size of 6.40 Å that is complimentary in size to CO_2 and favorable for its adsorption. The other gases, CH_4 and N_2, adsorb much less efficiently. n-ZIF-67 shows excellent performance not only for CO_2 adsorption but also for CO_2/N_2, CO_2/CH_4 and CH_4/N_2 separations from 1:1 ratio mixtures at different pressures from 1 to 20 bar, taking into account both the adsorption isotherm data set and breakthrough experiments. The selectivity for CH_4 over N_2 was very low, emphasizing the main impact of this material for CO_2 capture. Comparative adsorption experiments revealed consistently better adsorption and separation performance for the PEG-templated n-ZIF-67 compared to PEG-templated n-ZIF-8 or other ZIFs in the literature. The adsorption enthalpy data (Qst = 34.44 KJ/mol) obtained from highly correlated Langmuir model fitting revealed that CO_2 adsorption at n-ZIF-67 was driven by physical rather than chemical interactions at zero loading, consistent with the important role of the high specific surface area ultramicroporous structure (e.g. physical trapping) and polar interactions between the gas and the adsorbent. Adsorption-desorption cycling tests for CO_2 and CH_4 gas adsorption revealed excellent adsorbent stability with more than ca. 99.9% of the adsorption capacity remaining after 15 cycles. PEG-templated n-ZIF-8 that is obtained from a simple synthesis with low cost materials has the potential to be considered for economical production on a larger scale and is thus a promising physisorbent for CO_2 capture and separation.

Declaration of Competing Interest

The authors declare that they have no known competing financial interests or personal relationships that could have appeared to influence the work reported in this paper.

Data availability

No data was used for the research described in the article

Acknowledgment

Financial support for this study was provided by Universiti Kebangsaan Malaysia (UKM), under Geran Universiti Penyelidikan (GGPM-2022-067), ANR under reference ANR-20-CE05-0006, and the Deanship of Scientific Research at Majmaah University, Saudi Arabia. The authors would like to thank the Ministry of High Education and Research Fund of Tunisia.

REFERENCES

[1] S. Pacala, R. Socolow, Stabilization wedges: Solving the climate problem for the next 50 years with current technologies, Science. **305** (2004) 968-972, https://doi.org/10.1126/science.1100103.

[2] T. J. Crowley, Causes of climate change over the past 1000 years, Science. 289 (2000) 270-277, DOI: 10.1126/science.289.5477.270.

[3] D. Y. C. Leung, G. Caramanna, M. M. Maroto-Valer, An overview of current status of carbon dioxide capture and storage technologies, Renew. Sust. Energ. Rev. **39** (2014) 426-443, https://doi.org/10.1016/j.rser.2014.07.093.

[4] AL. Kohl, R. Nielson. Gas purification, fifthed, Gulf Publishing Company, Houston, 1997.

[5] E. B. Rinker, S. S. Ashour, O. C. Sandall, Absorption of carbon dioxide into aqueous blends of diethanolamine and methyldiethanolamine, Ind. Eng. Chem. Res. **39** (2000) 4346-4356, https://doi.org/10.1021/ie990850r.

[6] S. Cavenati, C. A. Grande, A. E. Rodrigues, Adsorption Equilibrium of Methane, Carbon Dioxide, and

Nitrogen on Zeolite 13X at High Pressures, J. Chem. Eng. Data. **49** (2004)1095–1101, https://doi.org/10.1021/je0498917.
[7] J. R. Li, R. J. Kuppler, H. C. Zhou, Selective gas adsorption and separation in metal-organic frameworks, Chem. Soc. Rev. 38 (2009) 1477–1504, https://doi.org/10.1039/B802426J.
[8] Y. He, W. Zhou, G. Qian, B. Chen, Methane storage in metal-organic frameworks, Chem. Soc. Rev. **43** (2014) 5657-5678, https://doi.org/10.1039/C4CS00032C.
[9] K. S. Park, Z. Ni, A. P. Côté, J. Y. Choi, R. Huang, F. J. Uribe-Romo, H. K. Chae, M. O'Keeffe, O. M. Yaghi, Exceptional chemical and thermal stability of zeolitic imidazolate frameworks, PNAS. **103** (2006) 10186-10191, https://doi.org/10.1073/pnas.0602439103.
[10] K. Zhou, B. Mousavi, Z. Luo, S. Phatanasri, S. Chaemchuen, F. Verpoort, Characterization and properties of Zn/Co zeolitic imidazolate frameworks vs. ZIF-8 and ZIF-67, J. Mater. Chem. A. **5** (2017) 952–957, https://doi.org/10.1039/C6TA07860E.
[11] X. Li, X. Gao, L. Ai, J. Jiang, Mechanistic insight into the interaction and adsorption of Cr(VI) with zeolitic imidazolate framework-67 microcrystals from aqueous solution, J. Chem. Eng. **274** (2015) 238-246, https://doi.org/10.1016/j.cej.2015.03.127.
[12] H. R. Abid, G. H. Pham, H. M. Ang, M. O. Tade, S. Wang, Adsorption of CH_4 and CO_2 on Zr-metal organic frameworks, J. Colloid. Interface. Sci. **366** (2012) 120-124, https://doi.org/10.1016/j.jcis.2011.09.060.
[13] Z. Liang, M. Marshall, A. L. Chaffee, CO_2 adsorption-based separation by metal organic framework (Cu-BTC) versus zeolite (13X), Energ Fuel. **23** (2009) 2785–2789, https://doi.org/10.1021/ef800938e.
[14] R. Banerjee, H. Furukawa, D. Britt, C. Knobler, M. O'Keeffe, O. M. Yaghi, Control of pore size and functionality in isoreticular zeolitic imidazolate frameworks and their carbon dioxide selective capture properties, J. Am. Chem. Soc. **131** (2009) 3875–3877, https://doi.org/10.1021/ja809459e.
[15] Z. Bao, L. Yu, Q. Ren, X. Lu, S. Deng, Adsorption of CO_2 and CH_4 on a magnesium-based metal organic framework, J. COLLOID. INTERF. SCI. **353** (2011) 549–556, https://doi.org/10.1016/j.jcis.2010.09.065.
[16] C. Volkringer, T. Loiseau, M. Haouas, F. Taulelle, D. Popov, M. Burghammer, C. Riekel, C. Zlotea, F. Cuevas, M. Latroche, D. Phanon, C. Knofelv, P.L. Llewellyn, G. Ferey, Occurrence of Uncommon Infinite Chains Consisting of Edge-Sharing Octahedra in a Porous Metal Organic Framework-Type Aluminum Pyromellitate Al4(OH)8[C10O8H2] (MIL-120): Synthesis, Structure, and Gas Sorption Properties, Chem. Mater. **21** (2009) 5783–5791, https://doi.org/10.1021/cm9023106.
[17] W. Morris, N. He, K. G. Ray, P. Klonowski, H. Furukawa, I. N. Daniels, Y. A. Houndonougbo, M. Asta, O. M. Yaghi, B. B. Laird, A combined experimental-computational study on the effect of topology on carbon dioxide adsorption in zeolitic imidazolate frameworks, J. Phys. Chem. C. **116** (2012) 24084–24090, https://doi.org/10.1021/jp307170a.
[18] D. Danaci, R. Singh, P. Xiao, P. A. Webley, Assessment of ZIF materials for CO2 capture from high pressure natural gas streams, J. Chem. Eng. **280** (2015) 486–493, https://doi.org/10.1016/j.cej.2015.04.090.
[19] S. K. Nune, P. K. Thallapally, A. Dohnalkova, C. Wang, J. Liuc, G. J. Exarhos, Synthesis and properties of nano zeolitic imidazolate frameworks, ChemComm. **46** (2010) 4878–4880, https://doi.org/10.1039/c002088e.
[20] J. McEwen, J. D. Hayman, A. Ozgur Yazaydin, A comparative study of CO2, CH4 and N2 adsorption in ZIF-8, Zeolite-13X and BPL activated carbon, Chem. Phys. **412** (2013) 72–76, https://doi.org/10.1016/j.chemphys.2012.12.012.
[21] R. Bose, J. Ethiraj, P. Sridhar, J. J. Varghese, N. S. Kaisare, P. Selvam, Adsorption of hydrogen and carbon dioxide in zeolitic imidazolate framework structure with SOD topology: experimental and modelling studies, Adsorption. **26** (2020) 1027–1038, https://doi.org/10.1007/s10450-020-00219-2.
[22] J. Ethiraj, S. Palla, H. Reinsch, Insights into high pressure gas adsorption properties of ZIF-67: Experimental and theoretical studies, Microporous Mesoporous Mater. **294** (2020) 109867, https://doi.org/10.1016/j.micromeso.2019.109867.
[23] N. Missaoui, H. Kahri, U.B. Demirci, Rapid room-temperature synthesis and characterizations of high-surface-area nanoparticles of zeolitic imidazolate framework-8 (ZIF-8) for CO_2 and CH_4 adsorption, J. Mater. Sci. **57** (2022) 16245-16257, https://doi.org/10.1007/s10853-022-07676-w.
[24] J. Qian, F. Sun, L. Qin, Hydrothermal synthesis of zeolitic imidazolate framework-67 (ZIF-67) nanocrystals, Mater. Lett. **82** (2012) 220-223, https://doi.org/10.1016/j.matlet.2012.05.077.
[25] C. Duan, Y. Yu, H. Hu, Recent progress on synthesis of ZIF-67-based materials and their application to heterogeneous catalysis, Green Energy Environ. **7** (2022) 3–15, https://doi.org/10.1016/j.gee.2020.12.023.
[26] E. Hunter-Sellars, P. A. Saenz-Cavazos, A. R. Houghton, S. R. McIntyre, I. P. Parkin, D. R. Williams, Sol–Gel Synthesis of High-Density Zeolitic Imidazolate Framework Monoliths via Ligand Assisted Methods: Exceptional Porosity, Hydrophobicity, and Applications in Vapor Adsorption. Adv. Funct. Mater., ***31***(2021), 2008357, https://doi.org/10.1002/adfm.202008357.
[27] D. Yu, L. Ge, B. Wu, L. Wu, H. Wang, T. Xu, Precisely tailoring ZIF-67 nanostructures from cobalt carbonate hydroxide nanowire arrays: Toward high-performance battery-type electrodes, J. Mater. Chem. A. **3** (2015)16688–16694, https://doi.org/10.1039/c5ta04509f.

[28] R. R. Kuruppathparambila, T. Josea, R. Babua, G. Y. Hwanga, A. C. Kathalikkattila, D. W. Kimb, D. W. Parka, A room temperature synthesizable and environmental friendly heterogeneous ZIF-67 catalyst for the solvent less and co-catalyst free synthesis of cyclic carbonates, Appl. Catal. B. **182** (2016) 562–569, https://doi.org/10.1016/j.apcatb.2015.10.005.
[29] B. Pattengale, S. Yang, J. Ludwig, Z. Huang, X. Zhang, J. Huang, Exceptionally Long-Lived Charge Separated State in Zeolitic Imidazolate Framework: Implication for Photocatalytic Applications, J. Am. Chem. Soc. **138** (2016) 8072-8075, https://doi.org/10.1021/jacs.6b04615.
[30] A. Gonzalez-Nelson, F. X. Coudert, M. A. van der Veen, Rotational dynamics of linkers in metal-organic frameworks, Nanomaterials. 9 (2019) 330, https://doi.org/10.3390/nano9030330
[31] K. Vellingiri, P. Kumar and A. Deep , K. H. Kim, Metal-organic frameworks for the adsorption of gaseous toluene under ambient temperature and pressure, Chem. Eng. J. **307** (2017) 1116-1126, https://doi.org/10.1021/jacs.6b04615.
[32] T.S. Anirudhan, P.G. Radhakrishnan, Thermodynamics and kinetics of adsorption of Cu (II) from aqueous solutions onto a new cation exchanger derived from tamarind fruit shell, J Chem Thermodyn. **40** (2008) 702-709, https://doi.org/10.1016/j.jct.2007.10.005.
[33] K. Y. Andrew Lin, H. Yang, W. D. Lee, Enhanced removal of diclofenac from water using a zeolitic imidazole framework functionalized with cetyltrimethylammonium bromide (CTAB), RSC Adv. **5** (2015) 81330–81340, https://doi.org/10.1039/c5ra08189k.
[34] W. Zhou, P. Wang, C. Li, Q. Huang, J. Wang, Y. Zhu, L. Fu, Y. Chenac, Y. Wu, CoSx/C hierarchical hollow nanocages from a metal-organic framework as a positive electrode with enhancing performance for aqueous supercapacitors. RSC Adv. **9** (2019)11253–11262, https://doi.org/10.1039/c9ra01167f.
[35] C. Chen, A. Wu, H. Yan, Y. Xiao, C. Tian, H. Fu, Trapping [PMo12O40]3- clusters into pre-synthesized ZIF-67 toward Mo: XCoxC particles confined in uniform carbon polyhedrons for efficient overall water splitting, Chem. Sci. **9** (2018) 4746–4755, https://doi.org/10.1039/c8sc01454j.
[36] K. Y. A. Lin, H. A. Chang, Ultra-high adsorption capacity of zeolitic imidazole framework-67 (ZIF-67) for removal of malachite green from water, Chemosphere. **139** (2015) 624–631, https://doi.org/10.1016/j.chemosphere.2015.01.041.
[37] R. Banerjee, A. Phan, B. Wang, C. Knobler, H. Furukawa, M. O'Keeffe, O. M. Yaghi, High-throughput synthesis of zeolitic imidazolate frameworks and application to CO_2 capture, Science. **319** (2008) 939–943, https://doi.org/10.1126/science.1152516.
[38] B. Ingham, M. F. Toney, 1-X-ray diffraction for characterizing metallic films, Metallic Films for Electronic, Optical and Magnetic Applications, Woodhead Publishing. (2014) 3-38, https://doi.org/10.1533/9780857096296.1.3.
[39] Z. Heydariyan, R. Monsef, M. Salavati-Niasari, Insights into impacts of Co3O4-CeO2 nanocomposites on the electrochemical hydrogen storage performance of g-C3N4: Pechini preparation, structural design and comparative study. Journal of Alloys and Compounds, **924** (2022) 166564, https://doi.org/10.1016/j.jallcom.2022.166564.
[40] M. Salavati-Niasari, F. Davar, Z. Fereshteh, Synthesis and characterization of ZnO nanocrystals from thermolysis of new precursor. Chemical engineering journal, 146 (2009) 498-502, https://doi.org/10.1016/j.cej.2008.09.042.
[41] G. K. Williamson, W. H. Hall. X-ray line broadening from filed aluminium and wolfram, Acta. metall, **1** (1953) 22-31, https://doi.org/10.1016/0001-6160 (53) 90006-6.
[42] X. Hou, H. Zhou, J. Zhang, Y. Cai, F. Huang, Q. Wie, High Adsorption Pearl-Necklace-Like Composite Membrane Based on Metal-Organic Framework for Heavy Metal Ion Removal, Part Part Syst Charact. **35** (2018) 1700438, doi:10.1002/ppsc.201700438.
[43] Y. Pan, H. Li, X. X. Zhang, Z. Zhang, X. S. Tong, C. Z. Jia, B. Liu, C. Y. Sun , L. Y. Yang, G. J. Chen, Large-scale synthesis of ZIF-67 and highly efficient carbon capture using a ZIF-67/glycol-2- methylimidazole slurry, Chem. Eng. Sci. **137** (2015) 504–514, https://doi.org/10.1016/j.ces.2015.06.069.
[44] Q. Zhou, L. Zhu, X. Xia, H. Tang, The water – resistant zeolite imidazolate framework 67 is a viable solid phase sorbent for fluoroquinolones while efficiently excluding macromolecules, Microchim. Acta. **183** (2016) 1839–1846, https://doi.org/10.1007/s00604-016-1814-7.
[45] Y. Pan, Y. Liu, G. Zeng, L. Zhao, Z. Lai, Rapid synthesis of zeolitic imidazolate framework-8 (ZIF-8) nanocrystalsin an aqueous system, ChemComm. **47** (2011) 2071–2073, https://doi.org/10.1039/c0cc05002d.
[46] J. Yan, B. Zhang, Z. Wang, Monodispersed ultramicroporous semi-cycloaliphatic polyimides for the highly efficient adsorption of CO_2, H_2 and organic vapors, Polym. Chem. **7** (2016) 7295–7303, https://doi.org/10.1039/c6py01734g.
[47] H. Hayashi, A. P. Côté, H. Furukawa, M. O'Keeffe, O. M. Yaghi, Zeolite A imidazolate frameworks, Nat Mater. **6** (2007) 501–506, https://doi.org/10.1038/nmat1927.
[48] H. Huang, W. Zhang, D. Liu, B. Liu, G. Chen, C. Zhong, Effect of temperature on gas adsorption and separation in ZIF-8: A combined experimental and molecular simulation study, Chem. Eng. Sci. **66** (2011) 6297–6305, https://doi.org/10.1016/j.ces.2011.09.009.

[49] J. Prez-Pellitero, H. Amrouche, F. R. Siperstein, G. Pirngruber, C. Nieto-Draghi, G. Chaplais, A. Simon-Masseron, D. Bazer-Bachi, D. Peralta, N. Bats, Adsorption of CO_2, CH_4, and N_2 on zeolitic imidazolate frameworks: Experiments and simulations, Chem. Eur. J. **16** (2010) 1560–1571, https://doi.org/10.1002/chem.200902144.

[50] J. A. Mason, K. Sumida, Z. R. Herm, R. Krishna, J. R. Long, Evaluating metal-organic frameworks for post-combustion carbon dioxide capture via temperature swing adsorption, Energy Environ. Sci. **4** (2011) 3030–3040, https://doi.org/10.1039/c1ee01720a.

[51] G. Ortiz, S. Brandès, Y. Rousselin, R. Guilard, Selective CO_2 Adsorption by a Triazacyclononane-Bridged Microporous Metal–Organic Framework, Chem. Eur. J. **17** (2011) 6689-6695, https://doi.org/10.1002/chem.201003680.

[52] Z. Zhang, Z. Li, and J. Li, Computational study of adsorption and separation of CO2, CH4, and N2 by an rht-type metal-organic framework, Langmuir, 28 (2012) 12122-12133, https://doi.org/10.1021/la302537d.

[53] P. Chowdhury, C. Bikkina, S. Gumma, Gas adsorption properties of the chromium-based metal organic framework MIL-101, J. Phys. Chem. C. **113** (2009) 6616–6621, https://doi.org/10.1021/jp811418r.

[54] P. Ammendola, F. Raganati, R. Chirone, CO2 adsorption on a fine activated carbon in a sound assisted fluidized bed: Thermodynamics and kinetics, Chem. Eng. J. **322** (2017) 302–313, https://doi.org/10.1016/j.cej.2017.04.037.

[55] T. S. Anirudhan, P. G. Radhakrishnan, Thermodynamics and kinetics of adsorption of Cu(II) from aqueous solutions onto a new cation exchanger derived from tamarind fruit shell, J. Chem. Thermodyn. **40** (2008) 702–709, https://doi.org/10.1016/j.jct.2007.10.005.

[56] B. Guo, L. Chang, K. Xie, Adsorption of Carbon Dioxide on Activated Carbon, J. Nat. Gas Chem. **15** (2006) 223–229, https://doi.org/10.1016/S1003-9953(06)60030-3.

[57] X. Zhou, H. Yi, X. Tang, H. Deng, H. Liu, Thermodynamics for the adsorption of SO_2, NO and CO_2 from flue gas on activated carbon fiber, Chem. Eng. J. **200** (2012) 399–404, https://doi.org/10.1016/j.cej.2012.06.013.

[58] S. Cavenati, C. A. Grande, A. E. Rodrigues, C. Kiener, U. Müller, Metal organic framework adsorbent for biogas upgrading, Ind. Eng. Chem. Res. **47** (2008) 6333–6335, https://doi.org/10.1021/ie8005269.

[59] Z. Zhang, P. Li, T. Zhao, Y. Xia, Enhanced CO_2 Adsorption and Selectivity of CO2/N2on Amine@ZIF-8 Materials, Adsorp Sci Technol. **2022** (2022) 1-12, https://doi.org/10.1155/2022/3207986.

[60] J. A. Dunne, M. Rao, S. Sircar, R. J. Gorte, A. L. Myers, Calorimetric heats of adsorption and adsorption isotherms. 2. O_2, N_2, Ar, CO_2, CH_4, C_2H_6, and SF_6 on NaX, H-ZSM-5, and Na-ZSM-5 zeolites. Langmuir, **12** (1996) 5896-5904, https://doi.org/10.1021/la960496r.

Highlights

- PEG-templated n-ZIF-67 exhibits high CO_2 adsorption capacity vs. n-ZIF-8
- CO_2/N_2 selectivity higher for n-ZIF-67 vs n-ZIF-8, especially at lower pressures
- Isosteric heat of adsorption data highlights favorable CO_2 selectivity for n-ZIF-67
- CO_2 physisorption process and constant cycling stability tests excellent 15-cycle reusability

Declaration of interests

☒ The authors declare that they have no known competing financial interests or personal relationships that could have appeared to influence the work reported in this paper.

☐The authors declare the following financial interests/personal relationships which may be considered as potential competing interests:

Declarations of interest: NONE

Author Contributions Statement

Nadhem Missaoui, Amani Chrouda: Formal analysis, Resources, Methodology, Writing - review& editing. **Hamza Kahri, Andrew J Gross,** Investigation, Writing-original draft. **Mohammad Rezaei Ardani:** Investigation, **Pang Ai Ling:** Conceptualization, Writing - review& editing. **Mohsen Ahmadipour:** Supervision, Funding acquisition, Conceptualization, Writing - review& editing.

PEG-templated synthesis of ultramicroporous n-ZIF-67 nanoparticles with high selectivity for the adsorption and uptake of CO_2 over CH_4 and N_2

Nadhem Missaoui[1*], Amani Chrouda[2,3*], Hamza Kahri[1,4], Andrew J. Gross[5], Mohammad Rezaei Ardani[6], Pang Ai Ling[7,8*], Mohsen Ahmadipour[9*]

[1] Laboratory of Interfaces and Advanced Materials, Faculty of Sciences, University of Monastir, Tunisia
[2]Departement of Chemistry, College of Science at Zulfi, Majmaah University, Zulfi 11952, Saudi Arabia
[3]Institut de Recherche sur l'Hydrogène, Université du Québec à Trois-Rivières, 3351, Boul. des Forges, C.P.500, Trois-Rivières (QC), Canada G9A5H7.
[4]Université de Poitiers, IC2MP UMR 7285 CNRS, 86073 09 Poitiers Cedex, France
[5]Département de Chimie Moléculaire (DCM), Univ. Grenoble Alpes-CNRS, 570 rue de la chimie, 38041 Grenoble, France.
[5]School of Materials and Mineral Resources Engineering, Universiti Sains Malaysia, Engineering Campus, 14300, Nibong Tebal, Pulau Pinang, Malaysia
[7]Department of Chemical Science, Faculty of Science, Universiti Tunku Abdul Rahman, Kampar, Perak, 31900, Malaysia
[8]Centre for Photonics and Advanced Materials Research, Universiti Tunku Abdul Rahman, Sungai Long Campus, Jalan Sungai Long, Bandar Sungai Long, Cheras, 43000 Kajang, Selangor, Malaysia
[6]Institute of Microengineering and Nanoelectronics, Universiti Kebangsaan Malaysia, 43600 Bangi, Selangor, Malaysia
*Corresponding author: mahmadipour@ukm.edu.my

Abstract

Challenges remain concerning the development of rapid and low-cost adsorbents that combine good separation performance with high adsorption capacity, especially for CO_2. Herein, we report for the first time a new polyethylene glycol templated synthesis method to obtain a nanocrystalline zeolitic imidazolate framework (n-ZIF-67) at room temperature in 5 minutes. The n-ZIF-67 nanoparticles were characterized using X-ray powder diffraction with Rietveld refinement (space group = I-43 m, a = 17.0545(4) Å), Fourier-transform infrared, transmission electron microscopy, thermogravimetric analysis, and N_2 adsorption (Brunauer-Emmett-Teller) measurements and exhibited excellent properties, including a total pore volume of 0.86 cm^3/g, a high surface area equal to 1891 m^2/g, and 0.64 nm size ultramicropores.). The highly porous ZIF-67 nanoparticles were explored for the adsorption and desorption of CH_4, CO_2, and N_2 gases at pressures up to 40 bar and isotherm temperatures of 273, 298, 323, and 353 K. The adsorption isotherms revealed a high capacity for CO_2 of 681 mg/g at 298 K and an adsorption enthalpy of 29.19 to 34.44 KJ/mol, in part linked to the ultramicroporous structure. The n-ZIF-67 particles exhibited gas uptake values for CH_4 and N_2 of 241 mg/g and 219 mg/g, respectively. As far as the authors are concerned, these are the highest capacities ever reported for zeolitic framework metal organic frameworks such as ZIF-67 and ZIF-8. The Langmuir adsorption isotherm was employed to obtain the maximum adsorption capacity, q_m, and adsorption equilibrium constant, K_L. The isosteric heat of adsorption data sheds light on a CO_2 physisorption process. The n-ZIF-67 also exhibited high CO_2/N_2 and CO_2/CH_4 mixed gases selectivity, with the preferential adsorption of CO_2 over N_2 or CH_4 confirmed by breakthrough experiments. The n-ZIF-67 with ultramicropores is therefore an effective new adsorbent for greenhouse gas capture with high CO_2 gas selectivity over competing gases. Zeolitic framework MOFs merit further development as low-cost and easy-to-synthesize adsorbents to help address the pressing need to mitigate CO_2 emissions.

Keywords
Gas Adsorption; Equilibrium; Carbon dioxide; Methane; Specific Surface Area; Zeolitic Imidazolate Framework; Selectivity.

1. Introduction

One of the biggest issues facing the world community is climate change brought on by global warming. The generation and accumulation of greenhouse gases in the atmosphere have mostly been caused by the emission of gases like methane (CH_4), carbon dioxide (CO_2), and nitrogen oxide (NO_2), and especially CO_2 [1-3]. The major industrial technologies used over the past few decades for separating and capturing CO_2 and CH_4 are, in general, based on absorption by solvents, membrane separation, and adsorption methods [4-6].

Adsorbents such as activated carbon and zeolites are among the most effective materials for gas separation in the chemical industry. Thanks to their large specific surface areas and pore volumes, crystalline porous metal-organic frameworks (MOFs) show great performance for gas adsorption and storage applications. MOFs are comprised of unique networks of metal ions or clusters that are coupled to organic ligands that give rise to unprecedented chemical and structure tunability. Numerous MOFs have been formed and investigated to date for CO_2 capture, CH_4 storage, and gas mixtures separation [7, 8]. MOFs can selectively adsorb gases owing to their unique pore sizes and geometries, as well as functional groups (e.g. via electrostatics) within the pores. Zeolitic imidazolate frameworks (ZIFs) are a class of MOFs that have been used extensively and have a tetrahedral network structure that is in many ways similar to zeolites, but with the important difference that they are constructed using transition metals associated with imidazolate ligands [9]. ZIFs, notably ZIF-67, have unique chemical, thermal, and water stabilities, that makes them promising candidates for industrial adsorption applications [10, 11]. Thanks to their high specific surface and pore geometries and chemistries, ZIFs are suitable adsorbents for CO_2 and CH_4 (Table 1) [12-23].

Several methods have been reported for the production of ZIF-67 with tunable porosity and morphology, such as sol-gel, solvothermal, microwave/ultrasound-assisted, and surfactant-assisted methods [24-26].
These methods permit the preparation of highly crystalline ZIF-67 with different crystallite sizes and porosities with some control, depending on factors such as synthesis time, temperature, and solvent [22, 24, 27]. Many require reaction times of several hours to days due to slow coordination interactions and discontinuities. For example, ZIF-67 crystals are typically obtained after 12 to 72 h using solvothermal methods at temperatures between 50-200°C [25]. It is therefore desirable to not only discover high-performance adsorbent materials, but also to discover materials that can be easily, economically and ecologically obtained, with a high level of control over crystal size and morphology (including phase purity). Nanocrystalline ZIF-67 with controlled morphology and particle size can be prepared using a polymer or surfactant template [19, 23]. The use of a template can prevent the formation of non-uniform agglomerates with large variations in sample size and morphology as well as larger particles [22]. Room temperature methods capable of generating ZIF-67 in a few hours are also desirable [28]. The diverse synthesis possibilities to obtain ZIF-67 with attractive chemical and physical properties has resulted in its use as a great material for catalysis [29], separation [30], and volatile organic compounds (VOCs) adsorption [31] applications. Nevertheless, the application and advantages of ZIF-67 for gas adsorption and separation have been rarely studied (see Table 1 for a detailed literature summary).

In this study, we report the facile and fast synthesis of ZIF-67 nanoparticles (NPs) in just a few minutes using N, N-dimethylformamide (DMF) as the solvent and polyethylene glycol (PEG) as a soft template. The use of PEG with a mild reaction temperature avoids the need for conventional high temperature solvothermal and microwave methods, while promoting the formation of homogeneous and stable ZIF-67 dispersions. To the best of our knowledge, the use of PEG as a template has not been reported previously for ZIF-67 synthesis. PEG was chosen over other polymer templates since it is low cost and has the capacity to generate a homogenous mixture comprising metallic salts thanks to its attractive solubility properties. During MOF synthesis, the polymer is

considered to adsorb onto the metal surface and alter the growth kinetics of colloids, allowing for the uniform growth of hexagonally-shaped particles [19, 23]. In these former examples, poly (diallyldimethylammonium chloride) and PEG were used for the production of ZIF-67 and ZIF-8, respectively. Following successful synthesis and characterization of PEG-templated ZIF-67 nanoparticles, we report here the gravimetric adsorption studies of CO_2, CH_4, and N_2 using PEG-templated n-ZIF-67 as well as PEG-templated n-ZIF-8 as adsorbents. The adsorption/desorption isotherms were achieved at temperatures of 273, 298, 323, and 353 K, at low and high pressures, and considered together with Langmuir modelling. Real-time dynamic breakthrough experiments of PEG-templated ZIF-67 for CO_2/N_2, CO_2/CH_4 and N_2/CH_4 mixtures are also reported.

2. Material and Methods

2.1. Synthesis of PEG-templated ZIF-8 nanoparticles (n-ZIF-8)

All the materials in this study were purchased from Sigma-Aldrich and were employed as received, including cobalt nitrate hexahydrate ($Co(NO_3)\cdot 6H_2O$; 99 %), 2-methylimidazole ($C_4H_6N_2$: mIm; 99 %), N,N-dimethylformamide (DMF; 99%), polyethylene glycol (PEG, average molecular weight = 20.000 $g.mol^{-1}$), triethylamine (TEA; $(C_2H_5)_3N$; 99%), and methanol (99 %). The microporous PEG-templated ZIF-8 ($Zn(Im)_2$) nanoparticles were obtained inaccordance with the procedures of our recently reported room-temperature method [23]. The ZIF-8 material was activated under vacuum at 423 K for 12 h prior to gas adsorption measurements. Table 1 summarizes the textural properties of ZIF-8 from our previous study.

2.2. Synthesis of PEG-templated ZIF-67 nanoparticles (n-ZIF-67)

ZIF-67 NPs were synthesized in a similar manner to the previous publication with some modification [23], i.e., $Co(NO_3)_2\cdot 6H_2O$ and mIm were used as precursors with PEG as a soft template. The choice of PEG was encouraged by its ability to form a homogenous solution with metallic salts thanks to micellar and dispersion effects to promote the uniform growth of particles with reduced particle size and agglomeration. In the first step, the PEG powder (0.4 g) was dispersed in 10 mL of DMF; $Co(NO_3)_2\cdot 6H_2O$ (1.4551 g, 5 mmol) was then added with slight stirring for 2 min at 298 K to form the Co-solution. Later, 2-methylimidazole (2.0525 g, 25 mmol) was dispersed in DMF (10 mL); TEA was used as a base and slowly added (6.75 mL) with stirring over 3 min to obtain the linker-solution. After complete dissolution, the Co-solution was mixed with the linker-solution and stirred for 5 min at room temperature. The purple precipitates were filtered, washed with ethanol to remove possible undissolved reagents including PEG, then collected via centrifugation (4000 rpm, 10 min). Finally, the obtained purple powder was dried in a vacuum oven at 423 K for 24 h to achieve the final product, ZIF-67 NP (herein referred to as n-ZIF-67).

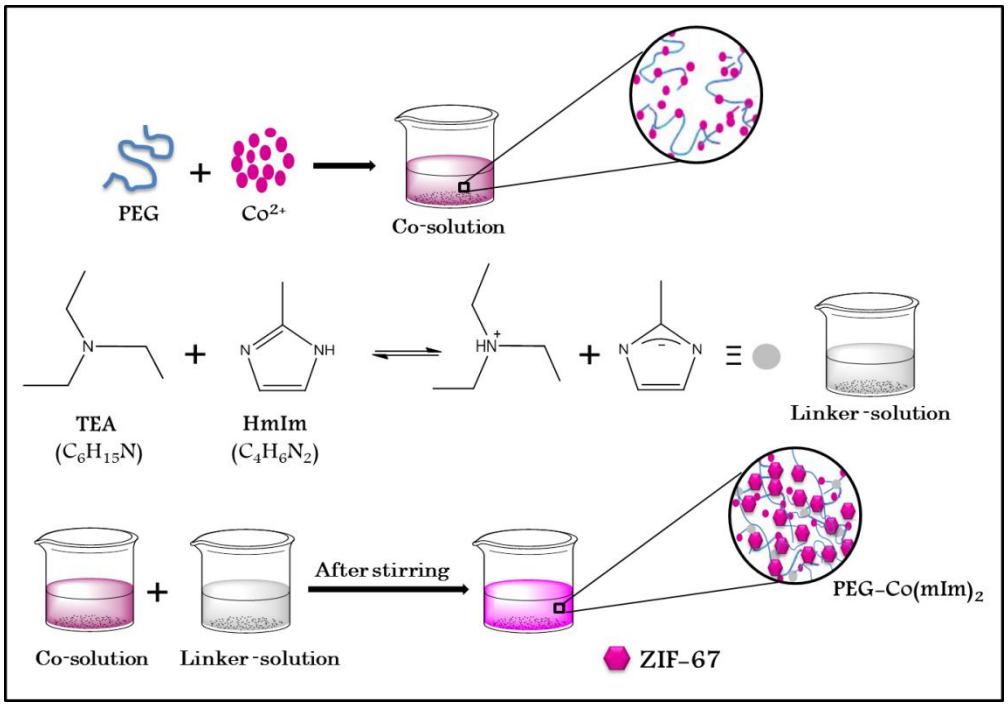

Scheme 1: Room temperature synthesis reaction to obtain PEG-template ZIF-67 (n-ZIF-67).

Table 1. Comparison of the CO_2 and CH_4 adsorption parameters diverse MOFs and ZIFs

ZIFs/ MOFs	Soft template	BET surface area m^2/g	Particle Size (nm)	Pore volume cm^3/g	Pore diameter (nm)	CO_2 adsorption (mg/g)	CH_4 adsorption (mg/g)	CO_2/CH_4 Selectivity	Ref
Zr-MOF[a]	none	1433	63	0.63	0.88	356.1 (273, 9.8 bar)	57.6 (273, 9.8 bar)	2.2-3.6	[12]
HKUST-1[b]	none	1571	-	0.79		558.8 (298 K, 15 bar)	73.6 (298 K, 15 bar)	-	[13]
ZIF-68[c], **69**[a]	none	1090, 950	-	-	1.03, 0.78	61.6-79.2 (298 K, 1bar)	102.4 (298 K, 1 bar)	5.5-5.6	[14]
Mg-MOF-74[e]	none	1174	5000-25000	0.648	1.02	360.8 (298 K, 1 bar)	16.0 (298 K, 1 bar)	-	[15]
MIL-120[f]	none	-	-	-	-	211.8 (303 K, 10 bar)	28.8 (303 K, 10 bar)	-	[16]
ZIF-93[g]	none	864	-	0.46	1.79	407 (298 K, 60 bar)	-	-	[17]
ZIF-11[h]	none	-	-	0.46	1.49	269.3 (298 K, 40 bar)	-	-	[17]
ZIF-7[i]	none	-	-	0.21	0.75	89.8 (298 K, 40 bar)	-	-	[17]
ZIF-71[j]	none	1025	1000-2000	-	1.65	356.4 (298 K, 45 bar)	-	-	[18]
ZIF-8[j]	PDADMAC[k]	1264	57	0.51	-	347.6(298 K, 40 bar)	-	-	[19]
ZIF-8	none	1475		0.70	-	36.1(298 K, 1 bar)	-	-	[20]
ZIF-8	none	1502	90	0.54	0.7-1.2	469.9 (298 K, 40 bar)	-	-	[21]
ZIF-67[l]	none	1478	500-1000	0.66	0.64-1.04	513.9 (298 K, 50 bar)	-	-	[22]
n-ZIF-8	PEG[m]	1694	150	0.67	0.787	51.5 (298 K, 1 bar)	36.0 (298 K, 1 bar)		
n-ZIF-8	PEG	1694	150	0.67	0.787	547.0 (298 K, 40 bar)	211.58 (298 K, 40 bar)	3.00-8.06	[23]
n-ZIF-67	PEG	1891	66	0.86	0.64	72.0 (298 K, 1bar)	49.0 (298 K, 1 bar)		This
n-ZIF-67	PEG	1891	66	0.86	0.64	681 (298 K, 40 bar)	241 (298 K, 40 bar)	3.67-16.05	work

[a]$Zr_6O_4(OH)_4(BDC)_6$ with BDC: 1,4-dicarboxybenzene; [b]$Cu_3(BTC)_2$ with BTC: benzene-1,3,5-tricarboxylic acid; [c]Zn(bIm)(nIm) with bIm: benzimidazole and nIm: 2-Nitroimidazole; [d]Zn(cbIm)(nIm) with cbIM: 5-chlorobenzimidazole; [e]$Zn_2(dhtp)(H_2O)_2.8H_2O$ with dhtp: 2,5-dihydroxyterephthalate; [f]$Al_4(OH)_8$(BTEC) with BTEC: 1,2 ,4,5-benzenetetracarboxylic acid ; [g]$Zn(almeIm)_2$ with almeIm: 4-methylimidazole-5-carbaldehyde; [h]$Zn(bIm)_2$ with bIm: benzimidazole; [i]$Zn(bIm)_2$; [j]$Zn(dcIm)_2$ with dcIm: 4,5-dichloroimidazole; [j]$Zn(mIm)_2$ with mIm: 2-methylimidazolate; [k]PDADMAC: poly(diallyldimethylammonium chloride) ; [l]$Co(mIm)_2$; [m]PEG as polyethylene glycol (average molecular weight = 20.000 g mol^{-1})

2.3. Characterization

FTIR spectroscopy was performed using a Perkin Elmer Spectrum Two instrument with attenuated total reflectance (ATR) spectra recorded from 4000 to 400 cm^{-1}. X-ray powder diffraction spectra (XRD) from 5° to 60° were recorded on a Bruker D8 Discover diffractometer with a scanning rate of 2°/min. The morphology and elemental composition of n-ZIF-67 was determined by transmission electron microscopy (TEM, Philips CM200) combined with an energy-dispersive X-ray spectrometer (EDX). The particle size analyses were determined using Image J software. Thermogravimetric analysis curves (TGA) were measured on a Mettler Toledo STARe apparatus by heating the samples from 298 K up to 973 K at a heating rate of 2°C/min under an air atmosphere. At 77 K, nitrogen adsorption-desorption isotherms (Micrometrics ASAP-2420 instrument; sample degassing at 423 K for 24 h under vacuum) were collected to determine the Brunauer-Emmett-Teller (BET) specific surface area (P/P° ranging from 0.01 to 0.35), total micropore volume (V_P), and pore size distribution (t-plot method).

2.3 CO_2, CH_4, and N_2 adsorption

Pure component adsorption isotherms of CO_2, CH_4, and N_2 at n-ZIF-67 and n-ZIF-8 were obtained by gravimetric analysis (Autosorb-iQ-MP analyzer) in the range of 0-40 bar at different temperatures: 273, 298, 323 and 353 K. The samples were degassed at 423 K under a high vacuum for 24 hours prior to the sorption measurement. The CO_2 used was of high purity (99.99%) and obtained from Sigma-Aldrich. The gases used wereall high purity (99.99%) and obtained from Sigma-Aldrich. Numerous adsorption kinetic models were employedto define the adsorption equilibrium isotherm data. In this work, the Langmuir adsorption kinetics model (Eq. (1)) was used to fit the equilibrium isotherm data [32]. This model was used to describe the monolayer pattern of the adsorbed layer on the homogeneous surface. The Langmuir equation can be expressed by the equilibrium adsorption capacity (q, mg/g), maximum adsorption capacity (q_m, mg/g), Langmuir isotherm constant or a parameter related to the affinity constant between adsorbate and adsorbent (K_L, L/g), and partial pressure (P, bar)as Eq. (1).

$$q = q_m \frac{k_L P}{1 + k_L P} \qquad \text{Eq. (1)}$$

3. Results and discussion

3.1 Structural analysis

The FTIR spectrum of the PEG templated n-ZIF-67 recorded between 400 and 4000 cm^{-1} is shown in Fig. 1. The n-ZIF-67 structure contains the ligand, mIm, which is responsible for most of the band characteristics. Precisely, the bands that appeared between 600 and 1500 cm^{-1} are ascribed to bending and stretching of the imidazole ring, such as the bands at 1145 and 1308 cm^{-1}, for the bending signal, and bands at 1415 and 1433 cm^{-1}, for the stretching vibrations [31, 33]. The bands at 994 and 750 cm^{-1} can be attributed to the bending vibrations of C–N and C–H, respectively, while the band at 694 cm^{-1} can be attributed to the bending variation of the mIm ring. The absorption band at 1637 cm^{-1} is due to the C=C stretch mode, whereas the absorption band at 1584 cm^{-1} is attributed to the stretching mode of C=N. The two small absorption bands at 2929 and 3136 cm^{-1} can be accredited to the asymmetric stretching modes of the aliphatic C–H and the aromatic ring of mIm, respectively. Interestingly, the

Co=N stretching vibration band is observed at 424 cm^{-1} [34], suggesting that the cobalt ions are linked chemically with nitrogen atoms of the methylimidazole (mIm) groups to shape the imidazolate. The FTIR results confirmed the successful synthesis of pure ZIF-67 [35].

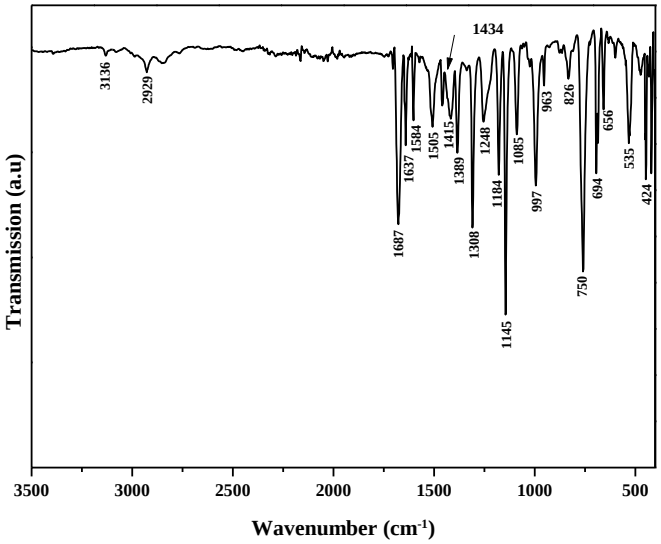

Fig.1. FTIR spectrum of n-ZIF-67.

As was mentioned in Section 2.2, n-ZIF-67 NPs were rapidly synthesized in minutes. The material was isolated in about 1 hr with the synthesis process occurring at room temperature and pressure. The method is rapid but also easily scalable, although with the notable downside that DMF and methanol solvents are used. The X- ray powder diffraction method was used for analyzing the chemical composition of as-produced n-ZIF-67 NPs. The sharp diffraction peaks at 2θ values of 7.4°, 10.4°, 12.8°, 14.7°, 16.5°, 18.0° and 19.5°, 22.1°, 24.5°, 26.7°, and 29.6° are assigned to the ZIF-67 planes of (011), (002), (112), (022), (013), (222), (114), (233), (134) and (044), respectively [36]. The XRD diffraction pattern with Rietveld refinement in Fig. 2 represents the common peaks of ZIF-67 and matches well with the simulated ZIF-67 diffractogram [36, 37]. Crystallite sizes were calculated using the Debye-Sherrer equation (Eq. 2) [38- 40]:

$$L = \frac{K\lambda}{\beta\cos\theta} \qquad \text{Eq. (2)}$$

Where L is the diameter of the crystallites (nm), K is the numerical Scherrer constant (0.93 Å), λ is the X-ray wavelength (1.54 Å), β is the full width at half-maximum intensity (FWHM) in radians, and θ is the Bragg diffraction angle. The crystallite size of n-ZIF-67 NPs was first determined using the Debye-Scherrer equation, equal to about 78 nm. The refined XRD structural parameters, calculated grain sizes, crystallite sizes and strains of n-ZIF-67 are collated in Table 2.

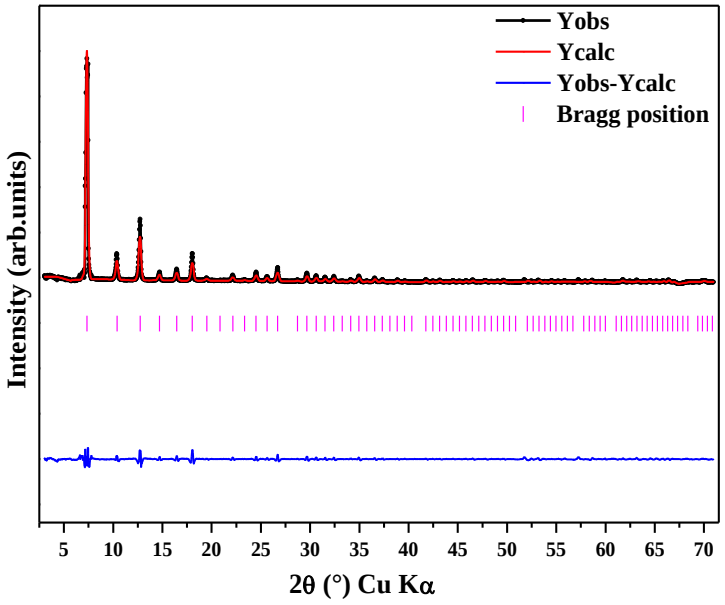

Fig.2: Rietveld plots of the XRD data for the PEG templated n-ZIF-67 $(Co(mIm)_2$ with the observed (black line), calculated (solid line), calculated Bragg reflection positions (vertical purple line), and the difference pattern between observed and calculated profiles (blue line, bottom).

Next, we considered the Williamson-Hall (W-H) method to determine the size for comparison with the Scherrer technique and TEM data. In the W-H method [41], the strain induced broadening arising from crystal imperfection and distortions is related by: $\beta_s = 4\varepsilon \tan(\theta)$ Eq. (3)

Here, ε is the root mean square value of the micro-strain, $\varepsilon = \frac{\Delta d}{d}$. Assuming that the particle size and strain contributions to line broadening are independent of each other and that both have a Cauchy like profile, the observed line breadth is simply the sum of the two: $\beta_{hkl} \cos(\theta) = \frac{k\lambda}{D} + 4\varepsilon \sin(\theta)$ Eq. (4)

A plot is drawn with $\sin(\theta)$ along the x-axis and $\beta_{hkl} \cos(\theta)$ along the y-axis for as-prepared PEG-templated n-ZIF-67 (Fig 3 (a)). The slope and y-intersect of the fitted line represent the strain and the particle size respectively. We can remark that the calculated crystallite size using the W-H technique (D_{W-H} = 91 nm) is larger than that calculated using Scherrer's technique (78 nm). This is due to the presence of strain which also contributes to the broadening of peaks. The grain sizes observed by TEM (see Fig. 3 and discussion below) are larger than those calculated by Scherrer's and W-H techniques. This can be explained by the fact that each particle observed by TEM is formed by several crystallized grains.

Table 2: Refined structural parameters and calculated grain sizes, crystallite sizes and strains of n-ZIF-

n-ZIF-67 [Co (mIm)$_2$]	Cubic
Space group	I -4 3 m
Cell parameters	a=b=c = 17.0545 (1) Å
Cell volume	4873.139 (2) Å^3
Discrepancy factors (%)	R_p = 0.339 R_F = 0.914 R_{wp} = 0.53 χ^2 = 1.94
Bragg R factor	1.34
D_{TEM} (nm)	~ 30 - 100
D_{sch} (nm)	78
D_{W-H} (nm)	~ 91
Strain (ε)	0.000325

The morphology of n-ZIF-67 was studied using TEM. According to Fig. 3 (b), the uniform rhombic dodecahedralmorphology was observed for ZIF-67 NPs, in agreement with a previous study of ZIF-67 nanocrystals [42]. The perfect crystalline structure of the synthesized n-ZIF-67 NPs was further confirmed by the well-defined rhombic facet and the clearly visible edge of ZIF-67. In addition, the surfaces of the particles appear regular and smooth, and the particles do not appear to be aggregated. Further interpretation of the TEM images using ImageJ software revealed that the particles had a Gaussian distribution, ranging from 30 to 100 nm, (Fig. 3 (c)), close to the size of the crystallites indicated via the Williamson-Hall data and the Debye-Scherrer equation (about 78 nm). The EDX analysis data, as shown in Fig. 3 (d), clearly demonstrates the expected elemental characteristic peaks for C (0.26 keV), N (0.53 keV), and Co (1, 6.9 keV), confirming the successful synthesis of ZIF-67 NPs.

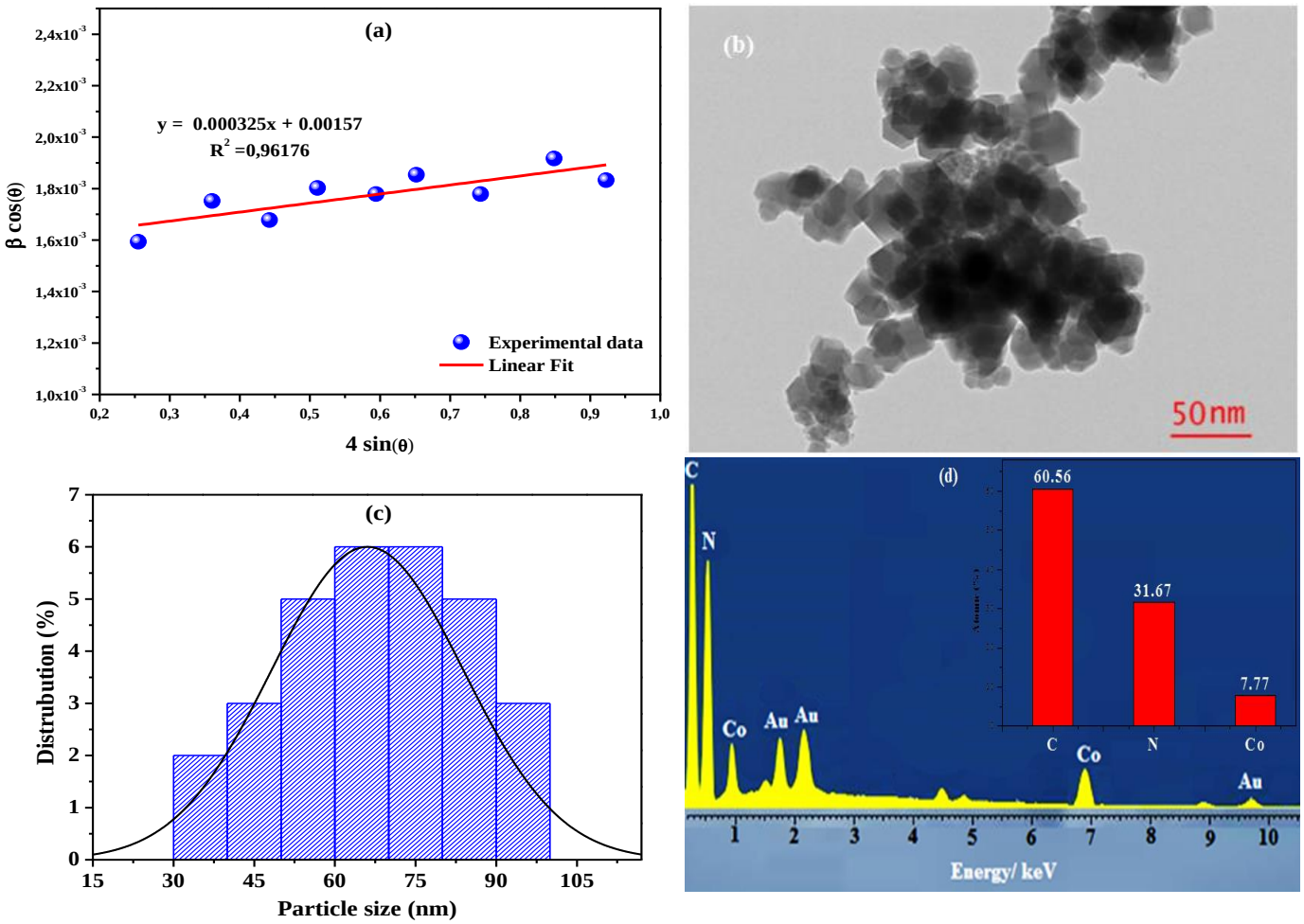

Fig.3. (a) strain graph of the cubic phase of n-ZIF-67 NPs (b) TEM image (c) TEM-based particle size distribution and (d) EDX spectrum

3.2. Thermal analysis

Thermal stability analysis of n-ZIF-67 NPs was conducted based on TGA curves. Fig. 4 depicts the weight loss rate and weight loss profiles. It is evident that a two-stage weight loss occurred at n-ZIF-8. The first weight loss was detected between 300 and 680 K, related to the removal of physisorbed molecules (e.g. H_2O, CO_2, and methanol) from the framework, concomitant with several exothermic peaks. The second weight loss at 700 K is followed by a rapid loss and exothermic peaks, which can be associated with the decomposition of the ZIF-67 NPs. The high thermal stability of ZIF-67 NPs, based on TGA curves, is consistent with previously reported data [34, 43, 44]. It was found that about 12 wt% of the initial weight of the powder remained after decomposition, which can be attributed to cobalt oxide, CoO, formation.

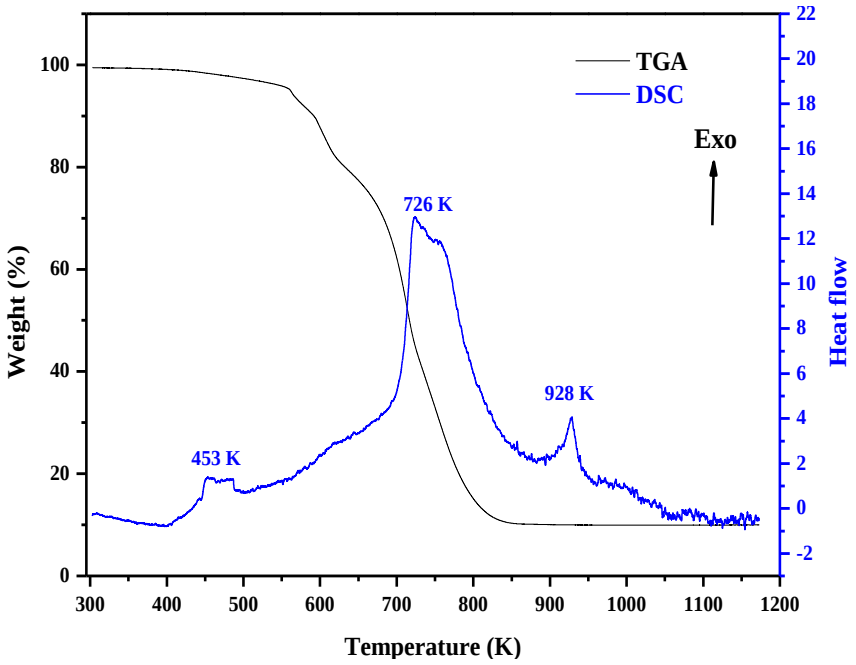

Fig.4. Thermal stability analysis of PEG-templated n-ZIF-67 (heating rate of 2°C/min; in air).

3.3. Nitrogen isotherm and pore size distribution

Considering-the TGA analysis data in Section 3.2, n-ZIF-67 NPs were degassed at 423 K prior to N_2 isotherm measurements. Fig. 5 displays the pore size distributions and N_2 adsorption isotherms for n-ZIF-67. As shownin Fig. 5 (a), the adsorbent showed a N_2 rapid uptake at a the very low relative pressure region ($10^{-5} < P/P° < 10^{-2}$). Based on the IUPAC classification, the sample had a typical type I isotherm [23, 35, 45] that confirms the microporosity of the material. As shown in Fig. 5, n-ZIF-67 NPs had reversible and reproducible N_2 adsorption and desorption isotherms, emphasising a stable material with permanent porosity and good rigidity. The BET method was employed to measure the sample porosity at $0.001 < P/P_0 < 0.35$. The BET surface area (S_{BET}) of the PEG-templated n-ZIF-67 NPs was 1871 m^2/g with a micropore volume of 0.86 cm^3/g, which are higher than previous values reported for ZIF-8 (including PEG-templated ZIF-8) and ZIF-67, as summarized in Table 1, highlighting the attractive adsorption potential of the new material reported here [23, 24]. The total pore volume (V_{micro}) of n-ZIF-67 was 0.86 cm^3/g at P/P° = 0.99. Fig. 5 (b) illustrates that the predominant pores of the MOF are 0.64 nm in diameter (ultramicropores). Such ultramicropores are expected to favor the adsorption of CO_2 molecules and eventually their preferential adsorption compared to N_2 and CH_4 molecules, based on geometric considerations (CH_4 (0.38 nm) > N_2 (0.364 nm) > CO_2 (0.33 nm)) [46].

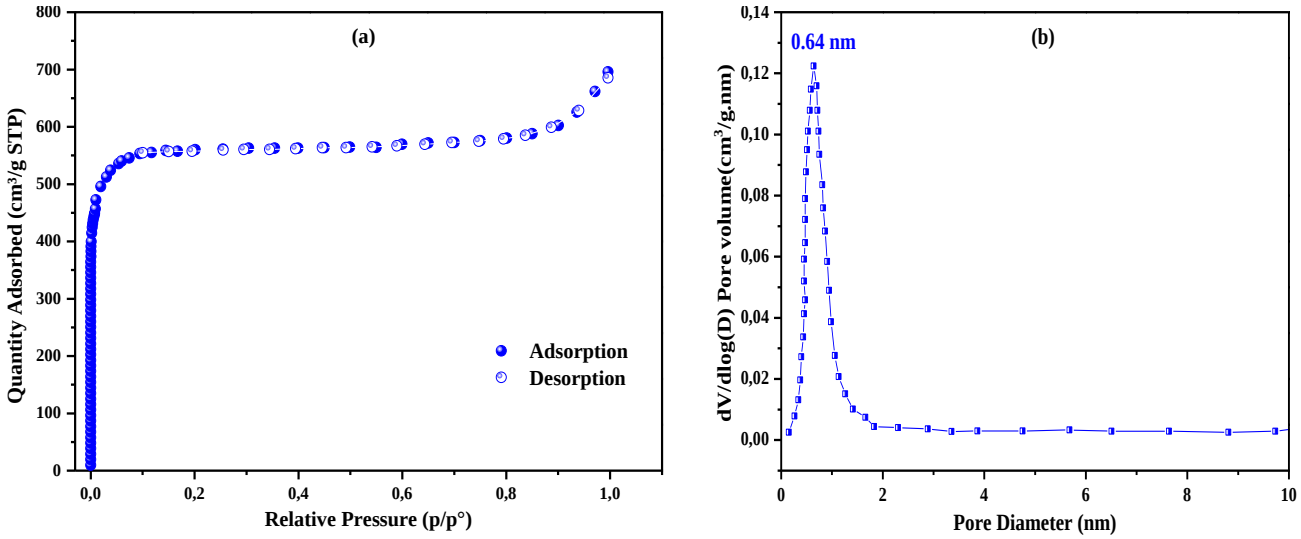

Fig. 5. (a) N_2 adsorption-desorption isotherms for n-ZIF-67, and (b) the corresponding pore sizedistribution.

3.4. CO_2, CH_4 and N_2 adsorption

The CO_2, CH_4, and N_2 adsorption isotherm performance at n-ZIF-67 and n-ZIF-8, with Langmuir adsorption model fitting, was subsequently investigated at low pressure (0 to 100 KPa/0 to 1 bar) and high pressure (0 to 40,000 KPa/0 to 40 bar) at different temperatures (273, 298, 323, and 253 K) after outgassing at 423 K. Nanoscale ZIF-67, due to its excellent textural properties including large porosity (microporosity and ultramicroporosity) and crystallinity, is an attractive candidate for the adsorption of gases such as CO_2, CH_4 and N_2, and especially the electrophile, CO_2, via interactions with its active adsorption sites within its pores [47, 23]. The high selectivity of ZIFs for CO_2 in gas mixtures, especially industrially important CO_2/N_2 and CO_2/CH_4 mixtures, is an attractive point that we endeavored to explore with PEG-templated n-ZIF-67. At low-pressure, between 0 and 100 KPa) and at different temperatures between 273 and 353 K, the CO_2 uptake of PEG-templated n-ZIF-67 increased quasi-linearly with increasing pressure (Fig. 5 (a)). At 100 KPa CO_2, the uptake did not reach saturation. According to the IUPAC classification, CO_2 and CH_4 exhibited a non-linear type I isotherm, which is in contrast to the N_2 isotherms which showed a linear adsorption behavior (Fig. 5 (a, c, and e)). In contrast, at PEG-templated n-ZIF-8, all of the gas adsorption isotherms exhibited a linear adsorption behavior (Fig. 5 (b, d, and f). The n-ZIF-67 particles showed a higher adsorption capacity for all gases at 100 KPa compared to n-ZIF-8. At 298 K and 100 KPa, the adsorption capacity of CO_2 at n-ZIF-67 was 111.89 mg (CO_2)/g, which was higher than the 51.5 mg(CO_2)/g recorded at PEG-templated n-ZIF-8 samples and ZIF-8 (Table 1) [20, 23]. The higher CO_2 capture capacity observed for n-ZIF-67 can be attributed, at least in part, to the combination of a higher BET surface area (1871 m^2/g) and pore volume (0.86 cm^3/g), and the ultramicropores below 0.7 nm (0.64 nm). Linked to the physical interactions of the free pore sites of ZIF-67 with CO_2 molecules, [49, 23], n-ZIF-67 adsorbed more CO_2 at 273 K (850.52 mg(CO_2)/g) than at higher temperatures such as 353 K (425.04 mg (CO_2)/g. An analogous behaviour has been observed and defined previously for ZIF-8, ZIF-69, and ZIF-76 [23, 49]. Additionally, the n-ZIF-67 material prepared here showed maximum adsorption capacities for CH_4 and N_2 of 40.72 mg(CH_4)/g for CH_4 and 23.02 mg(N_2)/g for N_2 at 298 K and 100 KPa (see Table 1). These adsorption capacities surpassour previous results with PEG-templated n-ZIF-8. This higher adsorption capacity for all three gases compared to n-ZIF-8 highlights the very promising physical characteristics of the newly synthesized n-ZIF-67 material.

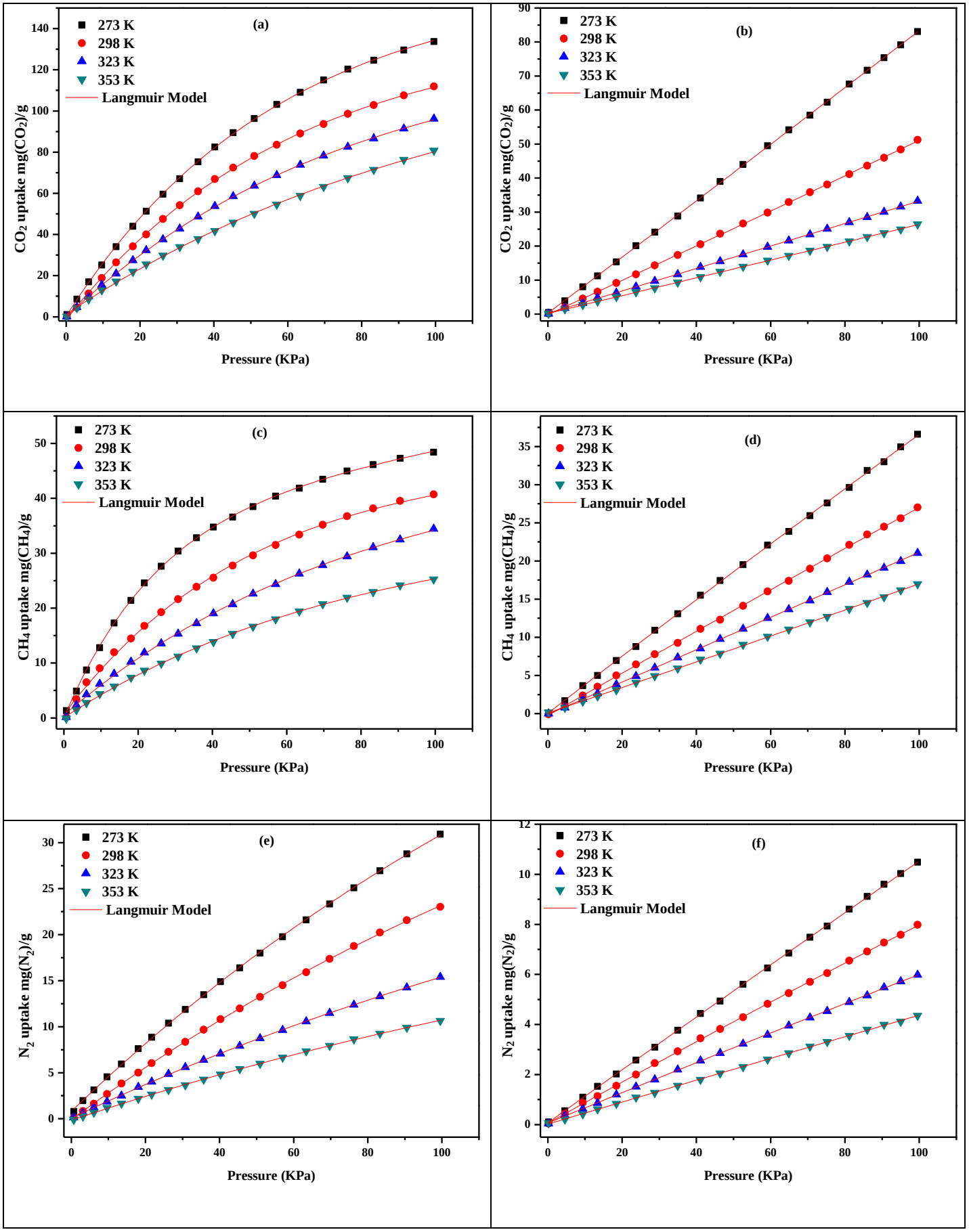

Fig. 6. CO_2, CH_4, and N_2 adsorption isotherms with Langmuir adsorption kinetic model fitting of n-ZIF-67 (a, c, e) versus n-ZIF-8 (b, d, f) at different temperatures (273, 298, 323, and 353K) and low pressure (0-1 bar)

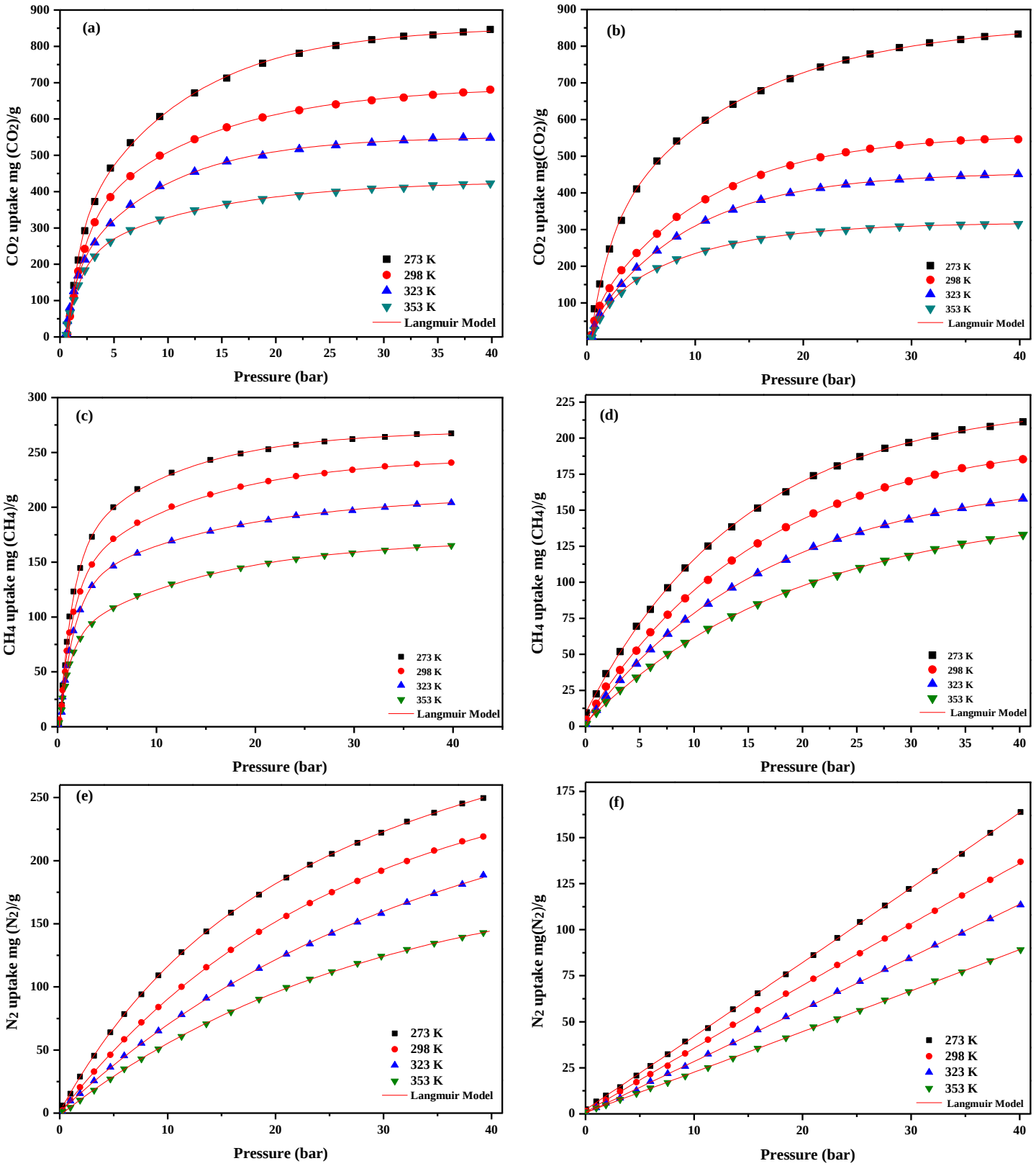

Fig. 7. CO_2, CH_4, and N_2 adsorption isotherms with Langmuir adsorption kinetic model fitting of n-ZIF-67 (a, c, e) with versus n-ZIF-8 (b, d, f) at different temperatures (273, 298, 323, and 353K) and high pressure (0-40 bar).

The adsorption isotherms of CO_2, CH_4, and N_2 at both n-ZIF-67 and n-ZIF-8 at various temperatures (273, 298, 323, and 353 K) and high pressure (0-40 bar) were also considered (Fig. 7). Generally, CO_2 and CH_4 adsorption increases with elevated pressure and the uptake reaches saturation at both materials. The N_2 uptake increases linearly with increasing pressure. The n-ZIF-67 samples showed significantly higher CO_2 adsorption capacity compared to CH_4 and N_2 adsorption, and higher adsorption capacities for all gases compared to n-ZIF-8 [23]. The adsorption capacity of 681 mg (CO_2)/g at n-ZIF-67 at 298 K and 40 bar CO_2 is the maximum capacity reported for a ZIF-67 and ZIF-8 adsorbent, as far as the authors are concerned (Table 1). The highest adsorption capacity achieved in this study was 846 mg (CO_2)/g at 40 bar for n-ZIF-67. This exceptional adsorption capacity at higher pressures further underlines the beneficial physical properties linked to the very large BET surface area and the ultramicropores of the n-ZIF-67 structure. Under the same conditions of 298 K and 40 bar, the adsorption capacities for CH_4 on n-ZIF-67 and n-ZIF-8 were 241 and 211.58 mg(CH_4)/g, respectively, while the N_2 adsorption capacities were 219 and 137 mg(N_2)/g, respectively. It is noted that at higher pressures, the N_2 isotherms revealed a quasi-linear behavior while the CO2 and CH4 isotherms showed type I behavior.

As discussed prior, according to the adsorption isotherms in Fig. 7, both n-ZIF-67 and n-ZIF-8 adsorbents had higher adsorption capacities for CO_2 compared to CH_4 and N_2. In addition to the smaller size of the molecule that corresponds well with the sub 1 nm micropores and especially the 0.64 nm ultramicropores of n-ZIF-67, CO_2 has an important quadrupole moment (13.4×10^{-40} C.m^2) compared to N_2 (4.7×10^{-40} C.m^2). These factors combined are consistent with better interactions via physisorption of CO2 at the surface of these zeolitic imidazolate frameworks MOFs, and especially n-ZIF-67 [50, 51]. The presence of a large quadruple moment in the CO_2 molecule can facilitate interactions with the electric field gradient inside pores as well as eventually short-range dipole-quadrupolar interactions. CH_4 on the other hand does not have a dipole or quadrupole moment but it does have a weak electric octuplet moment that could play a role in the adsorption of this gas [52].

Another factor to consider is that the three gases possess different electronic properties and therefore polarizabilities The greater polarizability of CH_4 molecules: 17.6×10^{-25} vs. 26.0×10^{-25} cm^3 for N_2 and CH_4, respectively can help to explain the better adsorption capacity of CH_4 compared to N_2 [53].

The adsorption isotherms of CO_2, CH_4, and N_2 for n-ZIF-67 and n-ZIF-8 fitted well to the Langmuir adsorption kinetics model (Eq. (1)). Table 3 shows the equation parameters used and the highly correlated correlation coefficient values for the data fitting according to the Langmuir model for n-ZIF-67. The maximum CO_2 adsorption capacity (q_m) according to the Langmuir adsorption model approach was also higher for n-ZIF-67 compared to n-ZIF-8 (Table 3). The value of the correlation coefficient highlights the slightly more homogeneous nature of the n-ZIF-67 adsorbent surface compared to ZIF-8 where values of R^2=0.996 were reported [23]. According to the Langmuir isotherm kinetic model, the q_m and K_L decreased at higher temperature, suggesting an exothermic adsorption process [23, 54].

Table 3 Equation parameters for the Langmuir isotherm model for PEG-templated n-ZIF-67

Adsorbate	T(K)	$Q_{m\ (mg.g^{-1})}$	$k_{L\ (L.\ g^{-1})}$	R^2
CO_2	273	854.48	1.98	0.998
	298	690.39	1.75	0.999
	323	551.40	1.62	0.999
	353	429.83	1.48	0.998
CH_4	273	269.67	1.46	0.999
	298	245.71	1.38	0.999
	323	211.02	1.29	0.999
	353	171.22	1.14	0.999
N_2	273	259.12	1.22	0.999
	298	229.32	1.16	0.999
	323	188.51	1.09	0.999
	353	142.98	0.98	0.999

The important characteristics of the Langmuir isotherm, the separation factor (R_L), can be represented by Eq. 5 [55].

$$R_L = \frac{1}{1+k_L P} \qquad \text{Eq. (5)}$$

Where K_L is the Langmuir constant and P (bar) is the pressure. For $R_L = 0$ (K_L is very large), irreversible adsorption; for $R_L = 1$ ($K_L = 0$), linear adsorption; for $0 < R_L < 1$, favorable and $R_L < 1$ ($K_L < 0$), unfavorable adsorption (that is, desorption). The values of R_L for all gases were determined over a wide pressure range and the results are shown in Fig. 8. All the R_L values are between 0 and 1, indicating that all three gases (CO_2, CH_4, N_2) are favorably adsorbed at n-ZIF-67 in the studied pressure range from 0 to 40 bar.

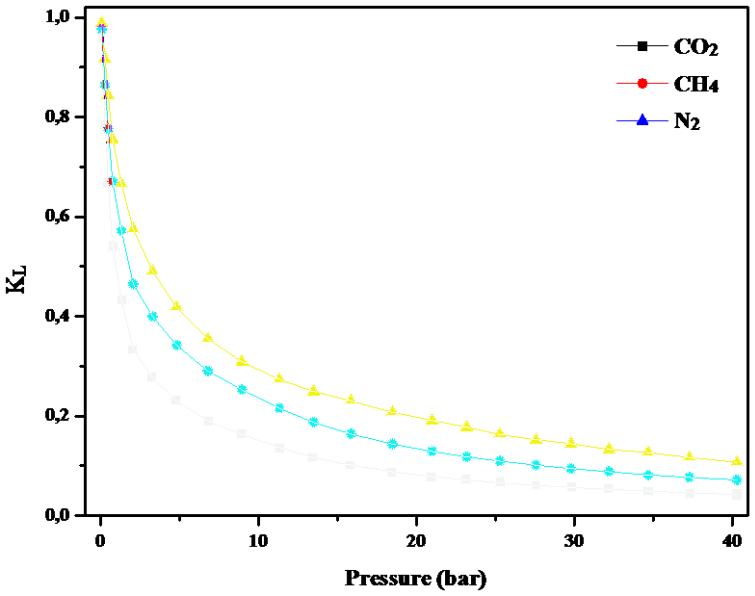

Fig. 8. Separation factor (R_L) plot against pressure for gas adsorption at n-ZIF-67.

3.5. Isosteric Heat of Adsorption

The isosteric heat of adsorption (Q_{st}) is an important parameter in gas adsorption studies. It allows us to understand how the adsorbent and adsorbate interact. According to the Langmuir kinetic model, the adsorption enthalpy of CO_2 at PEG-templated n-ZIF-67 was estimated from the experimental adsorption isotherms determined at different temperatures. From the Langmuir fitting parameters (Table 3), the adsorption enthalpy was calculated, following

the Clausius-Clapeyron equation (Eq. (6)) [56]

$$Qst = -RT^2 \left(\frac{d\ln(P)}{dT}\right) \qquad \text{Eq. (6)}$$

In which: T (K) is the temperature; P is the pressure (bar); R (8.314 J mol^{-1} K^{-1}) is the universal gas constant and Q_{st} is the heat of adsorption in KJ/mol. Based on the general hypothesis that the enthalpy of adsorption is independent of the temperature, the combination of equation 6 offers:

$$\ln P = \left(\frac{Qst}{RT}\right) + C \qquad \text{Eq. (7)}$$

In which: C is the constant.

In this study, the heat/enthalpy of adsorption (Q_{st}) of CO_2, CH_4, and N_2 were determined by linear plotting of the logarithm of the pressure (ln (P)) versus the reverse of the temperature (1/T) by using the equilibrium isotherm data. Fig. 9 (a) shows the heat of adsorption for all gases at zero loading for both n-ZIF-67 and n-ZIF8 frameworks Fig. 9 (b) shows Q_{st} as a function of the CO_2 uptake. The Q_{st} value is associated with different forces depending on the nature of the interaction between adsorbent-adsorbate, such as Van der Waals forces, dipole-dipole and dipole-quadrupole interactions, and chemical bonds.

According to the work of Zhou et al. [57], the Q_{st} value for physisorption is lower than 80 KJ/mol, while, it is between 80 and 200 kJ/mol for chemisorption. The heat of adsorption at zero loading for both samples, n-ZIF-67 and n-ZIF-8, are presented in Fig .9 (a). For the studied gases, the heats of adsorption were higher at n-ZIF-67 compared to n-ZIF-8. This corresponds well with a stronger interaction between the adsorbates and the ultramicropores in n-ZIF-67 framework. The largest relative increase in Qst between the two types of ZIF structures was observed for CO_2. The CO_2 gas, with its quadrupole moment, is considered especially strongly interacting with the ultramicropores in n-ZIF-67. For n-ZIF-67 and n-ZIF-8, the heats of adsorption at zero loading of CO_2 were 34.44 KJ/mol and 27.60 KJ/mol, respectively. The Q_{st} values attained for both adsorbents were less than 80 KJ/mol, indicating that the gas adsorption processes were controlled by physical rather than chemical adsorption.

Fig. 9 (b) shows the variation of the heat of adsorption values at 298 K for CO_2, CH_4, and N_2 at ~~on~~ n-ZIF-67. At low adsorption pressure, the heat of adsorption of CO_2 was greater than for either CH_4 or N_2. With an increase in adsorption uptake, the heat of CO_2 adsorption was reduced, owing to a decrease in the number of active adsorption sites as a result of the firm interaction of CO_2 with the ultramicroporous structure for n-ZIF-67, the enthalpy of adsorption for CO_2 was 34.44 KJ/mol at zero loading and 29.19 KJ/mol at high loading. Consequently, the enthalpy of adsorption of CO_2 decreases when the CO_2 adsorption capacity increases; this behavior is linked to the surface heterogeneity of the MOF [23]. In the low pressure region, the CO_2 gas also showed the highest heat of adsorption, thanks in part to its quadrupole moment. CO_2 demonstrated negligible variation in the heat of adsorption with loading, while CH_4 displayed a significant decrease in the heat of adsorption from about 26.51 KJ/mol at zero loading to about 24.99 KJ/mol at a loading of *ca.* 30 mg(CH_4)/g. Furthermore, the heat of adsorption for N_2 at n-ZIF-67 was independent of the N_2 uptake, indicating a weak interaction between N_2 and the n-ZIF-67 material. With regard to the other gases, it is evident that the heat of adsorption of CH_4 and N_2 on n-ZIF-67 was lower than that of CO_2. The data globally confirms the favorable selectivity of the n-ZIF-67 adsorbent for CO_2/CH_4 and CO_2/N_2, respectively.

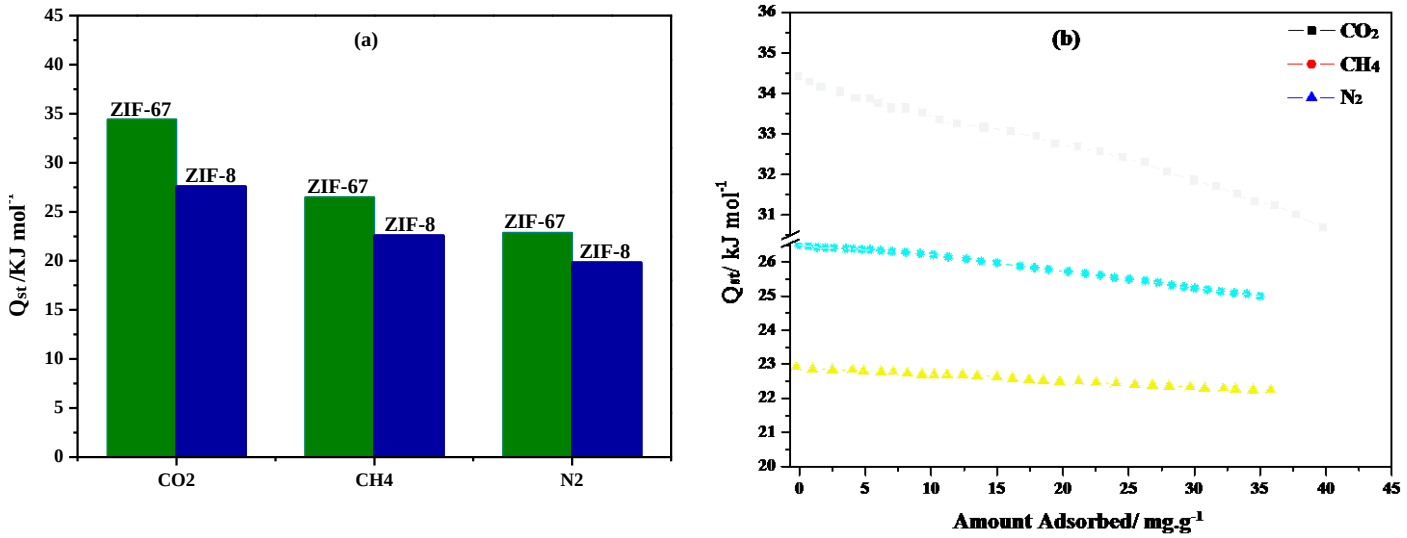

Fig. 9. (a) Comparison of the isosteric heats of adsorption at zero loading at 298 K for CO_2, CH_4 and N_2 at n-ZIF-67 and n-ZIF-8; (b) Variation in the heat of adsorption with loading at n-ZIF-67.

3.6. Selectivity of CO_2/N_2, CH_4/N_2 and CO_2/CH_4 on ZIF-67 NP

The gas selectivity behavior of PEG-templated n-ZIF-8 for CO_2/N_2 CO_2/CH_4 and CH_4/N_2 at n-ZIF-67 was evaluated and is shown in Fig. 10. First we estimated the selectivity by dividing the adsorption capacity of CO_2 by that of N_2 or CH_4 at each pressure point [13, 23, 58]. It is evident from Fig. 10 that ZIF-67's selectivity decreased as the pressure increased for CO_2 over N_2, CO_2 over CH_4, and CH_4 over N_2. Especially in the low-pressure region, the adsorption selectivity for CO_2 from CO_2/N_2 and CO_2/CH_4 mixtures at n-ZIF-67 was consistently higher than that of ZIF-8 materials, as reported in the literature [23, 59]. The n-ZIF-67 selectivity towards CO_2 at 298 K decreased slowly as the pressure was increased. Because of the low heat of adsorption of CO_2 at low pressure, the n-ZIF-67 exhibited lower selectivity towards CO_2 (at 298 K) compared, for example, to zeolite 13X (Q_{st} = 49 KJ/mol) [60]. On the other hand, a lower value is probably beneficial in reducing adsorbent regeneration energy requirements [60]. Furthermore, the CO_2/N_2 selectivity on n-ZIF-67 was maximized in the low-pressure range. As mentioned earlier, CO_2 has a smaller molecular size (3.3 Å), higher polarizability (26.3×10^{-25} cm^3), and a larger quadrupole moment (13.4×10^{-40} $C.m^2$) compared to molecular N_2 (3.8 Å; 17.6×10^{-25} cm^3 and 4.7×10^{-40} $C.m^2$, respectively), that supports the stronger interaction between the active adsorption sites within the ultramicropores of ZIF-67 and the CO_2 adsorbate, which is favorable for CO_2/N_2 separation. Particularly at 0.01, 20, and 40 bar, the CO_2/N_2 selectivity of n-ZIF-67 was up to 28, 11, and 6, respectively, which was higher compared to report ZIF-8 structures [23, 59]. When pressures were low, up to approximately 1 bar, and at 298 K, n-ZIF-67 exhibited a better selectivity for CO_2 over CH_4, with selectivity ranging from 13, at about 1 bar, to 15, at 0.5 bar. The CO_2/N_2 selectivity ranges from 6 to 28, whereas the CO_2/CH_4 selectivity ranges from 4 to 16, which are almost higher than those observed at ZIF-8 [23]. Moreover, with increasing pressure, the selectivity performance decreased. The selectivity for CH_4/N_2 was very low, nearly close to 1. Overall, these selectivity measurements show a high potential for CO_2 separation from CO_2/N_2 or CO_2/CH_4 gas mixtures by gas adsorption at higher pressures.

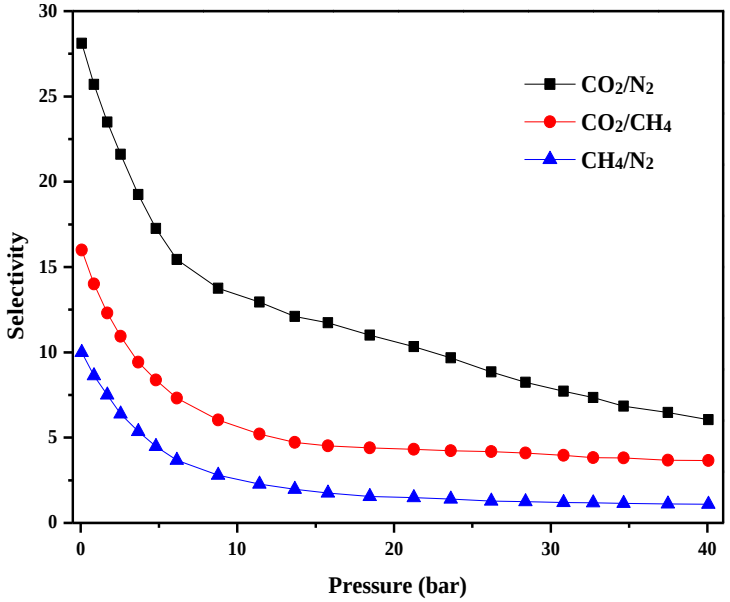

Fig.10. CO_2/N_2, CO_2/CH_4 and CH_4/N_2 selectivity's for n-ZIF-67 at 298 K.

3.7. Breakthrough experiments

In order to confirm the separation performance of PEG-templated n-ZIF-67 for 1:1 ratio CO_2/N_2, CO_2/CH_4 and N_2/CH_4 mixtures, real-time dynamic breakthrough experiments were carried out at 298 K and in the pressure region of 1-10 bar. As shown in Fig. 11 (a,b, c), the breakthrough profiles for the CO_2/N_2 (50/50, v/v) and CO_2/CH_4 (50/50, v/v) mixtures further verify that n-ZIF-67 prefers to adsorb CO_2 over N_2 or CH_4. Importantly, PEG-templated n-ZIF-67 is capable of completely separating CO_2/N_2 (50/50) and CO_2/CH_4 (50:50) mixtures. In addition, it can be seen that N_2 breaks through the fixed n-ZIF-67 adsorbent in a few seconds (Fig. 11 (a), (b) and (c)), revealing a small amount of N_2 is adsorbed. Comparing Fig. 11 (a) with Fig. 11 (b) and (c), we can highlight that the difference in breakthrough time between CO_2 and N_2 is larger than that of the breakthrough time observed between CO_2 and CH_4, and CH_4 and N_2, respectively. It is evident that PEG-templated ZIF-67 has greater CO_2/N_2 selectivity compared to CO_2/CH_4 and CH_4/N_2 selectivity, which is in accordance with the selectivity results obtained in Section 3.6 and Fig.10.

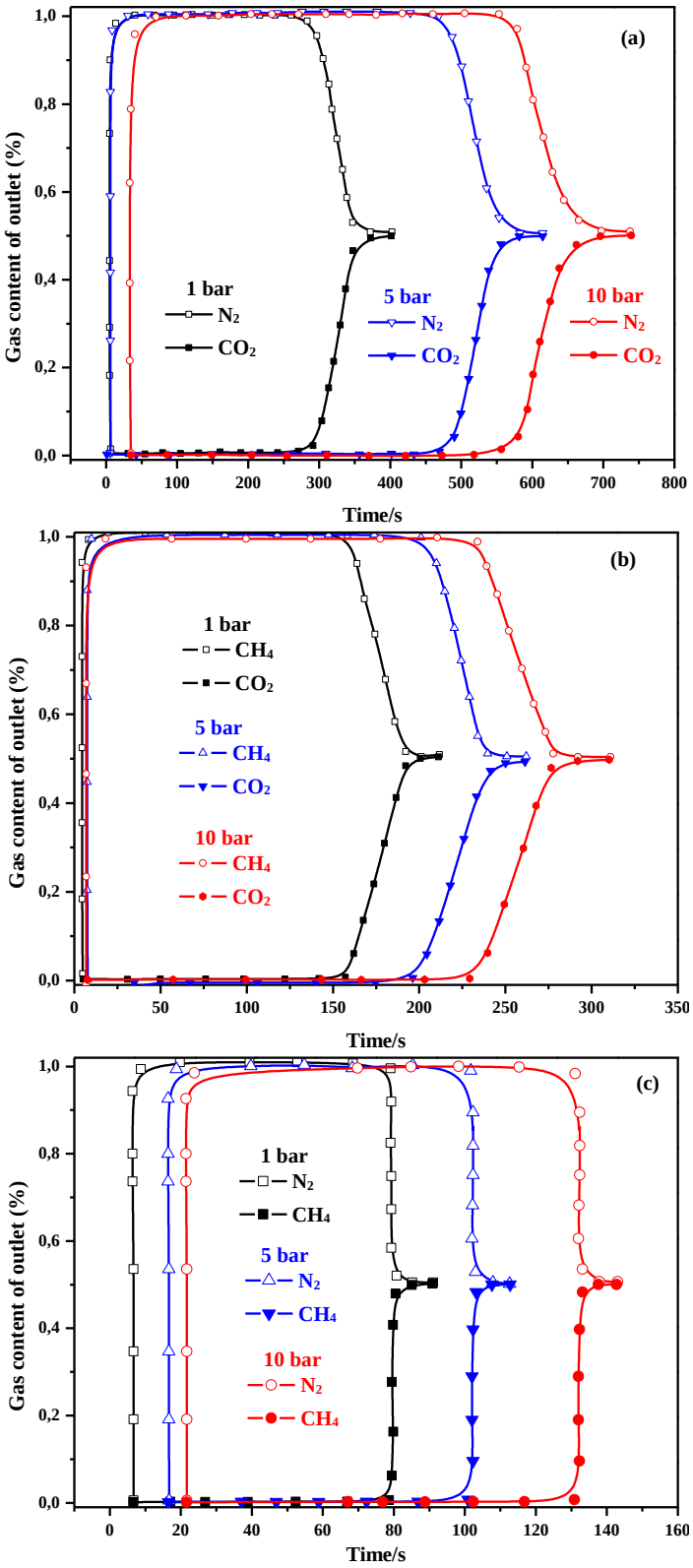

Fig. 11. Breakthrough curves of binary mixtures for (a) CO_2/N_2 (50/50, v/v), (b) CO_2/CH_4 (50/50, v/v), (c) CH_4/N_2 (50/50, v/v) separation experiments with PEG-templated n-ZIF-67 at pressures of 1, 10, 20 bar at 298 K.

3.8. Adsorption/desorption cycles

The adsorption stability of the n-ZIF-67 adsorbent was subsequently evaluated by prolonged cyclic CO_2 and CH_4 adsorption-desorption cycles (15 cycles of adsorption and regeneration). The adsorbents were heated to 423 K (10 K/min) under N_2 gas (50 mL/min) after each adsorption to release any adsorbed gases that remained on the surface of n-ZIF-67. The adsorbent was then cooled to 298 K while being maintained under N_2, and the weight was measured. A subsequent CO_2 adsorption was performed to continue the cycling test. The percentage ratio of the adsorption capacity of the regenerated adsorbent to the fresh one is defined as the adsorption index (AI) and is determined by the equation as follows:

$$AI = \frac{q_n}{q_1} \times 100 \qquad \text{Eq. (8)}$$

Where, q_1 and q_n indicate the CO_2 and CH_4 adsorption capacity of the first cycle and the n^{th} (n = 1-15) cycle, respectively.

The adsorption stability of n-ZIF-67 can be considered as its recyclability. The n-ZIF-67 adsorbent was used/reused over 15 cycles of successive CO_2 adsorption and desorption under the specified condition of 298 K and 40 bar of CO_2 gas (Fig. 12 (a)). It was stated earlier that the CO_2 adsorption capacity of as-prepared n-ZIF-67 was 681 mg (CO_2)/g (100%). In the second cycle, this value dropped to 680.2 mg (CO_2)/g (99.88%). After each cycle, the CO_2 adsorption capacity of n-ZIF-67 was very slightly reduced. The capacity was 679.6 mg (CO_2)/g by the end of the 15^{th} cycle (99.79%). This reduction should be related to the material loss as a result of the recycling process. Nevertheless, the CO_2 adsorption capacity after 15 cycles was still higher than 99%,which confirms the high reusability of the n-ZIF-67 adsorbent. Moreover, the CO_2 adsorption and desorption cycle curves were similar, suggesting the strong stability of n-ZIF-67 and appropriateness of this material for CO_2 adsorption. The extended cyclic CH_4 adsorption on n-ZIF-67 adsorbent was also conducted, and the results are shown in Fig. 12 (b). The results show that the adsorption capacity only decreased from 100% to 99.91% by the end of the 15^{th} cycle, signifying that most CH_4 molecules can also be successfully desorbed throughout the regeneration operation.

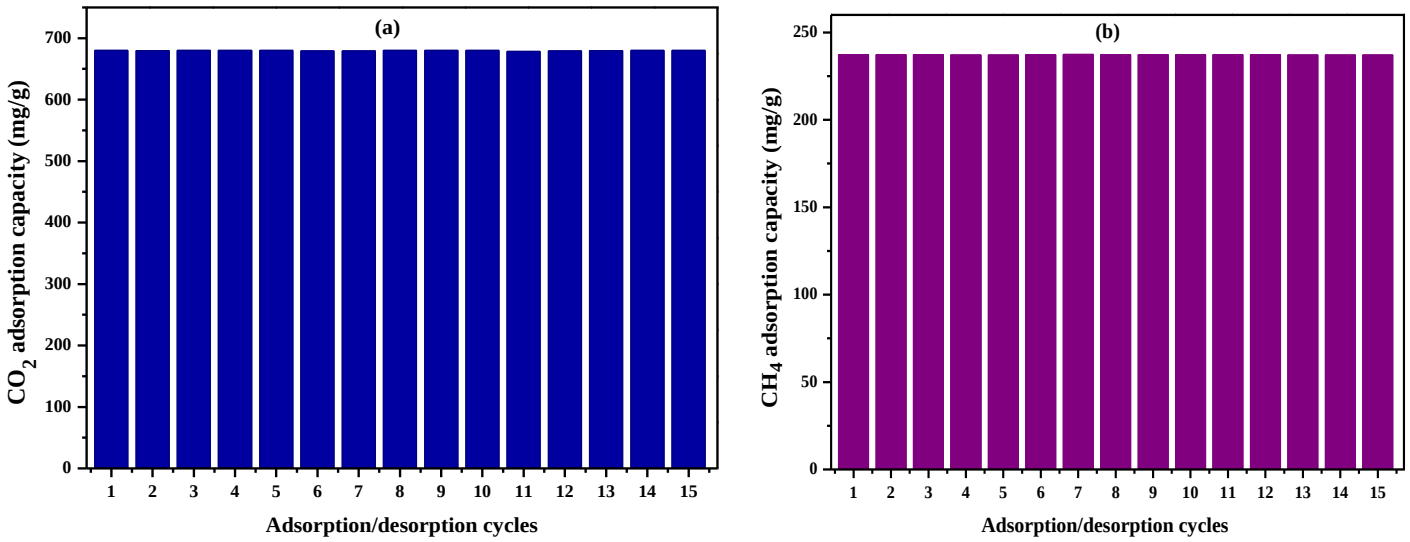

Fig. 12: CO_2 and CH_4 adsorption cycles of ZIF-67 NPs adsorbents.

Conclusion

In summary, PEG-templated hexagonal n-ZIF-67 nanoparticles were successfully synthesized for the first time via a simple and rapid protocol at room temperature. The adsorbent benefits from a very high BET surface of 1891 m^2/g, a large pore volume of 0.86 cm^3/g, and an average ultramicropore size of 6.40 Å that is complimentary in size to CO_2 and favorable for its adsorption. The other gases, CH_4 and N_2, adsorb much less efficiently. n-ZIF-67 shows excellent performance not only for CO_2 adsorption but also for CO_2/N_2, CO_2/CH_4 and CH_4/N_2 separations from 1:1 ratio mixtures at different pressures from 1 to 20 bar, taking into account both the adsorption isotherm data set and breakthrough experiments. The selectivity for CH_4 over N_2 was very low, emphasizing the main impact of this material for CO_2 capture. Comparative adsorption experiments revealed consistently better adsorption and separation performance for the PEG-templated n-ZIF-67 compared to PEG-templated n-ZIF-8 or other ZIFs in the literature. The adsorption enthalpy data (Qst = 34.44 KJ/mol) obtained from highly correlated Langmuir model fitting revealed that CO_2 adsorption at n-ZIF-67 was driven by physical rather than chemical interactions at zero loading, consistent with the important role of the high specific surface area ultramicroporous structure (e.g. physical trapping) and polar interactions between the gas and the adsorbent. Adsorption-desorption cycling tests for CO_2 and CH_4 gas adsorption revealed excellent adsorbent stability with more than ca. 99.9% of the adsorption capacity remaining after 15 cycles. PEG-templated n-ZIF-8 that is obtained from a simple synthesis with low cost materials has the potential to be considered for economical production on a larger scale and is thus a promising physisorbent for CO_2 capture and separation.

Declaration of Competing Interest

The authors declare that they have no known competing financial interests or personal relationships that could have appeared to influence the work reported in this paper.

Data availability

No data was used for the research described in the article

Acknowledgment

Financial support for this study was provided by Universiti Kebangsaan Malaysia (UKM), under Geran Universiti Penyelidikan (GGPM-2022-067), ANR under reference ANR-20-CE05-0006, and the Deanship of Scientific Research at Majmaah University, Saudi Arabia. The authors would like to thank the Ministry of High Education and Research Fund of Tunisia.

REFERENCES

[1] S. Pacala, R. Socolow, Stabilization wedges: Solving the climate problem for the next 50 years with current technologies, Science. **305** (2004) 968-972, https://doi.org/10.1126/science.1100103.

[2] T. J. Crowley, Causes of climate change over the past 1000 years, Science. 289 (2000) 270-277, DOI: 10.1126/science.289.5477.270.

[3] D. Y. C. Leung, G. Caramanna, M. M. Maroto-Valer, An overview of current status of carbon dioxide capture and storage technologies, Renew. Sust. Energ. Rev. **39** (2014) 426-443, https://doi.org/10.1016/j.rser.2014.07.093.

[4] AL. Kohl, R. Nielson. Gas purification, fifthed, Gulf Publishing Company, Houston, 1997.

[5] E. B. Rinker, S. S. Ashour, O. C. Sandall, Absorption of carbon dioxide into aqueous blends of diethanolamine and methyldiethanolamine, Ind. Eng. Chem. Res. **39** (2000) 4346-4356, https://doi.org/10.1021/ie990850r.

[6] S. Cavenati, C. A. Grande, A. E. Rodrigues, Adsorption Equilibrium of Methane, Carbon Dioxide, and

Nitrogen on Zeolite 13X at High Pressures, J. Chem. Eng. Data. **49** (2004)1095–1101, https://doi.org/10.1021/je0498917.
[7] J. R. Li, R. J. Kuppler, H. C. Zhou, Selective gas adsorption and separation in metal-organic frameworks, Chem. Soc. Rev. 38 (2009) 1477–1504, https://doi.org/10.1039/B802426J.
[8] Y. He, W. Zhou, G. Qian, B. Chen, Methane storage in metal-organic frameworks, Chem. Soc. Rev. **43** (2014) 5657-5678, https://doi.org/10.1039/C4CS00032C.
[9] K. S. Park, Z. Ni, A. P. Côté, J. Y. Choi, R. Huang, F. J. Uribe-Romo, H. K. Chae, M. O'Keeffe, O. M. Yaghi, Exceptional chemical and thermal stability of zeolitic imidazolate frameworks, PNAS. **103** (2006) 10186-10191, https://doi.org/10.1073/pnas.0602439103.
[10] K. Zhou, B. Mousavi, Z. Luo, S. Phatanasri, S. Chaemchuen, F. Verpoort, Characterization and properties of Zn/Co zeolitic imidazolate frameworks vs. ZIF-8 and ZIF-67, J. Mater. Chem. A. **5** (2017) 952–957, https://doi.org/10.1039/C6TA07860E.
[11] X. Li, X. Gao, L. Ai, J. Jiang, Mechanistic insight into the interaction and adsorption of Cr(VI) with zeolitic imidazolate framework-67 microcrystals from aqueous solution, J. Chem. Eng. **274** (2015) 238-246, https://doi.org/10.1016/j.cej.2015.03.127.
[12] H. R. Abid, G. H. Pham, H. M. Ang, M. O. Tade, S. Wang, Adsorption of CH_4 and CO_2 on Zr-metal organic frameworks, J. Colloid. Interface. Sci. **366** (2012) 120-124, https://doi.org/10.1016/j.jcis.2011.09.060.
[13] Z. Liang, M. Marshall, A. L. Chaffee, CO_2 adsorption-based separation by metal organic framework (Cu-BTC) versus zeolite (13X), Energ Fuel. **23** (2009) 2785–2789, https://doi.org/10.1021/ef800938e.
[14] R. Banerjee, H. Furukawa, D. Britt, C. Knobler, M. O'Keeffe, O. M. Yaghi, Control of pore size and functionality in isoreticular zeolitic imidazolate frameworks and their carbon dioxide selective capture properties, J. Am. Chem. Soc. **131** (2009) 3875–3877, https://doi.org/10.1021/ja809459e.
[15] Z. Bao, L. Yu, Q. Ren, X. Lu, S. Deng, Adsorption of CO_2 and CH_4 on a magnesium-based metal organic framework, J. COLLOID. INTERF. SCI. **353** (2011) 549–556, https://doi.org/10.1016/j.jcis.2010.09.065.
[16] C. Volkringer, T. Loiseau, M. Haouas, F. Taulelle, D. Popov, M. Burghammer, C. Riekel, C. Zlotea, F. Cuevas, M. Latroche, D. Phanon, C. Knofelv, P.L. Llewellyn, G. Ferey, Occurrence of Uncommon Infinite Chains Consisting of Edge-Sharing Octahedra in a Porous Metal Organic Framework-Type Aluminum Pyromellitate Al4(OH)8[C10O8H2] (MIL-120): Synthesis, Structure, and Gas Sorption Properties, Chem. Mater. **21** (2009) 5783–5791, https://doi.org/10.1021/cm9023106.
[17] W. Morris, N. He, K. G. Ray, P. Klonowski, H. Furukawa, I. N. Daniels, Y. A. Houndonougbo, M. Asta, O. M. Yaghi, B. B. Laird, A combined experimental-computational study on the effect of topology on carbon dioxide adsorption in zeolitic imidazolate frameworks, J. Phys. Chem. C. **116** (2012) 24084–24090, https://doi.org/10.1021/jp307170a.
[18] D. Danaci, R. Singh, P. Xiao, P. A. Webley, Assessment of ZIF materials for CO2 capture from high pressure natural gas streams, J. Chem. Eng. **280** (2015) 486–493, https://doi.org/10.1016/j.cej.2015.04.090.
[19] S. K. Nune, P. K. Thallapally, A. Dohnalkova, C. Wang, J. Liuc, G. J. Exarhos, Synthesis and properties of nano zeolitic imidazolate frameworks, ChemComm. **46** (2010) 4878–4880, https://doi.org/10.1039/c002088e.
[20] J. McEwen, J. D. Hayman, A. Ozgur Yazaydin, A comparative study of CO2, CH4 and N2 adsorption in ZIF-8, Zeolite-13X and BPL activated carbon, Chem. Phys. **412** (2013) 72–76, https://doi.org/10.1016/j.chemphys.2012.12.012.
[21] R. Bose, J. Ethiraj, P. Sridhar, J. J. Varghese, N. S. Kaisare, P. Selvam, Adsorption of hydrogen and carbon dioxide in zeolitic imidazolate framework structure with SOD topology: experimental and modelling studies, Adsorption. **26** (2020) 1027–1038, https://doi.org/10.1007/s10450-020-00219-2.
[22] J. Ethiraj, S. Palla, H. Reinsch, Insights into high pressure gas adsorption properties of ZIF-67: Experimental and theoretical studies, Microporous Mesoporous Mater. **294** (2020) 109867, https://doi.org/10.1016/j.micromeso.2019.109867.
[23] N. Missaoui, H. Kahri, U.B. Demirci, Rapid room-temperature synthesis and characterizations of high-surface-area nanoparticles of zeolitic imidazolate framework-8 (ZIF-8) for CO_2 and CH_4 adsorption, J. Mater. Sci. **57** (2022) 16245-16257, https://doi.org/10.1007/s10853-022-07676-w.
[24] J. Qian, F. Sun, L. Qin, Hydrothermal synthesis of zeolitic imidazolate framework-67 (ZIF-67) nanocrystals, Mater. Lett. **82** (2012) 220-223, https://doi.org/10.1016/j.matlet.2012.05.077.
[25] C. Duan, Y. Yu, H. Hu, Recent progress on synthesis of ZIF-67-based materials and their application to heterogeneous catalysis, Green Energy Environ. **7** (2022) 3–15, https://doi.org/10.1016/j.gee.2020.12.023.
[26] E. Hunter-Sellars, P. A. Saenz-Cavazos, A. R. Houghton, S. R. McIntyre, I. P. Parkin, D. R. Williams, Sol–Gel Synthesis of High-Density Zeolitic Imidazolate Framework Monoliths via Ligand Assisted Methods: Exceptional Porosity, Hydrophobicity, and Applications in Vapor Adsorption. Adv. Funct. Mater., ***31***(2021), 2008357, https://doi.org/10.1002/adfm.202008357.
[27] D. Yu, L. Ge, B. Wu, L. Wu, H. Wang, T. Xu, Precisely tailoring ZIF-67 nanostructures from cobalt carbonate hydroxide nanowire arrays: Toward high-performance battery-type electrodes, J. Mater. Chem. A. **3** (2015)16688–16694, https://doi.org/10.1039/c5ta04509f.

[28] R. R. Kuruppathparambila, T. Josea, R. Babua, G. Y. Hwanga, A. C. Kathalikkattila, D. W. Kimb, D. W. Parka, A room temperature synthesizable and environmental friendly heterogeneous ZIF-67 catalyst for the solvent less and co-catalyst free synthesis of cyclic carbonates, Appl. Catal. B. **182** (2016) 562–569, https://doi.org/10.1016/j.apcatb.2015.10.005.
[29] B. Pattengale, S. Yang, J. Ludwig, Z. Huang, X. Zhang, J. Huang, Exceptionally Long-Lived Charge Separated State in Zeolitic Imidazolate Framework: Implication for Photocatalytic Applications, J. Am. Chem. Soc. **138** (2016) 8072-8075, https://doi.org/10.1021/jacs.6b04615.
[30] A. Gonzalez-Nelson, F. X. Coudert, M. A. van der Veen, Rotational dynamics of linkers in metal-organic frameworks, Nanomaterials. 9 (2019) 330, https://doi.org/10.3390/nano9030330
[31] K. Vellingiri, P. Kumar and A. Deep , K. H. Kim, Metal-organic frameworks for the adsorption of gaseous toluene under ambient temperature and pressure, Chem. Eng. J. **307** (2017) 1116-1126, https://doi.org/10.1021/jacs.6b04615.
[32] T.S. Anirudhan, P.G. Radhakrishnan, Thermodynamics and kinetics of adsorption of Cu (II) from aqueous solutions onto a new cation exchanger derived from tamarind fruit shell, J Chem Thermodyn. **40** (2008) 702-709, https://doi.org/10.1016/j.jct.2007.10.005.
[33] K. Y. Andrew Lin, H. Yang, W. D. Lee, Enhanced removal of diclofenac from water using a zeolitic imidazole framework functionalized with cetyltrimethylammonium bromide (CTAB), RSC Adv. **5** (2015) 81330–81340, https://doi.org/10.1039/c5ra08189k.
[34] W. Zhou, P. Wang, C. Li, Q. Huang, J. Wang, Y. Zhu, L. Fu, Y. Chenac, Y. Wu, CoSx/C hierarchical hollow nanocages from a metal-organic framework as a positive electrode with enhancing performance for aqueous supercapacitors. RSC Adv. **9** (2019)11253–11262, https://doi.org/10.1039/c9ra01167f.
[35] C. Chen, A. Wu, H. Yan, Y. Xiao, C. Tian, H. Fu, Trapping [PMo12O40]3- clusters into pre-synthesized ZIF-67 toward Mo: XCoxC particles confined in uniform carbon polyhedrons for efficient overall water splitting, Chem. Sci. **9** (2018) 4746–4755, https://doi.org/10.1039/c8sc01454j.
[36] K. Y. A. Lin, H. A. Chang, Ultra-high adsorption capacity of zeolitic imidazole framework-67 (ZIF-67) for removal of malachite green from water, Chemosphere. **139** (2015) 624–631, https://doi.org/10.1016/j.chemosphere.2015.01.041.
[37] R. Banerjee, A. Phan, B. Wang, C. Knobler, H. Furukawa, M. O'Keeffe, O. M. Yaghi, High-throughput synthesis of zeolitic imidazolate frameworks and application to CO_2 capture, Science. **319** (2008) 939–943, https://doi.org/10.1126/science.1152516.
[38] B. Ingham, M. F. Toney, 1-X-ray diffraction for characterizing metallic films, Metallic Films for Electronic, Optical and Magnetic Applications, Woodhead Publishing. (2014) 3-38, https://doi.org/10.1533/9780857096296.1.3.
[39] Z. Heydariyan, R. Monsef, M. Salavati-Niasari, Insights into impacts of Co3O4-CeO2 nanocomposites on the electrochemical hydrogen storage performance of g-C3N4: Pechini preparation, structural design and comparative study. Journal of Alloys and Compounds, **924** (2022) 166564, https://doi.org/10.1016/j.jallcom.2022.166564.
[40] M. Salavati-Niasari, F. Davar, Z. Fereshteh, Synthesis and characterization of ZnO nanocrystals from thermolysis of new precursor. Chemical engineering journal, 146 (2009) 498-502, https://doi.org/10.1016/j.cej.2008.09.042.
[41] G. K. Williamson, W. H. Hall. X-ray line broadening from filed aluminium and wolfram, Acta. metall, **1** (1953) 22-31, https://doi.org/10.1016/0001-6160 (53) 90006-6.
[42] X. Hou, H. Zhou, J. Zhang, Y. Cai, F. Huang, Q. Wie, High Adsorption Pearl-Necklace-Like Composite Membrane Based on Metal-Organic Framework for Heavy Metal Ion Removal, Part Part Syst Charact. **35** (2018) 1700438, doi:10.1002/ppsc.201700438.
[43] Y. Pan, H. Li, X. X. Zhang, Z. Zhang, X. S. Tong, C. Z. Jia, B. Liu, C. Y. Sun , L. Y. Yang, G. J. Chen, Large-scale synthesis of ZIF-67 and highly efficient carbon capture using a ZIF-67/glycol-2- methylimidazole slurry, Chem. Eng. Sci. **137** (2015) 504–514, https://doi.org/10.1016/j.ces.2015.06.069.
[44] Q. Zhou, L. Zhu, X. Xia, H. Tang, The water – resistant zeolite imidazolate framework 67 is a viable solid phase sorbent for fluoroquinolones while efficiently excluding macromolecules, Microchim. Acta. **183** (2016) 1839–1846, https://doi.org/10.1007/s00604-016-1814-7.
[45] Y. Pan, Y. Liu, G. Zeng, L. Zhao, Z. Lai, Rapid synthesis of zeolitic imidazolate framework-8 (ZIF-8) nanocrystalsin an aqueous system, ChemComm. **47** (2011) 2071–2073, https://doi.org/10.1039/c0cc05002d.
[46] J. Yan, B. Zhang, Z. Wang, Monodispersed ultramicroporous semi-cycloaliphatic polyimides for the highly efficient adsorption of CO_2, H_2 and organic vapors, Polym. Chem. **7** (2016) 7295–7303, https://doi.org/10.1039/c6py01734g.
[47] H. Hayashi, A. P. Côté, H. Furukawa, M. O'Keeffe, O. M. Yaghi, Zeolite A imidazolate frameworks, Nat Mater. **6** (2007) 501–506, https://doi.org/10.1038/nmat1927.
[48] H. Huang, W. Zhang, D. Liu, B. Liu, G. Chen, C. Zhong, Effect of temperature on gas adsorption and separation in ZIF-8: A combined experimental and molecular simulation study, Chem. Eng. Sci. **66** (2011) 6297–6305, https://doi.org/10.1016/j.ces.2011.09.009.

[49] J. Prez-Pellitero, H. Amrouche, F. R. Siperstein, G. Pirngruber, C. Nieto-Draghi, G. Chaplais, A. Simon-Masseron, D. Bazer-Bachi, D. Peralta, N. Bats, Adsorption of CO_2, CH_4, and N_2 on zeolitic imidazolate frameworks: Experiments and simulations, Chem. Eur. J. **16** (2010) 1560–1571, https://doi.org/10.1002/chem.200902144.

[50] J. A. Mason, K. Sumida, Z. R. Herm, R. Krishna, J. R. Long, Evaluating metal-organic frameworks for post-combustion carbon dioxide capture via temperature swing adsorption, Energy Environ. Sci. **4** (2011) 3030–3040, https://doi.org/10.1039/c1ee01720a.

[51] G. Ortiz, S. Brandès, Y. Rousselin, R. Guilard, Selective CO_2 Adsorption by a Triazacyclononane-Bridged Microporous Metal–Organic Framework, Chem. Eur. J. **17** (2011) 6689-6695, https://doi.org/10.1002/chem.201003680.

[52] Z. Zhang, Z. Li, and J. Li, Computational study of adsorption and separation of CO2, CH4, and N2 by an rht-type metal-organic framework, Langmuir, 28 (2012) 12122-12133, https://doi.org/10.1021/la302537d.

[53] P. Chowdhury, C. Bikkina, S. Gumma, Gas adsorption properties of the chromium-based metal organic framework MIL-101, J. Phys. Chem. C. **113** (2009) 6616–6621, https://doi.org/10.1021/jp811418r.

[54] P. Ammendola, F. Raganati, R. Chirone, CO2 adsorption on a fine activated carbon in a sound assisted fluidized bed: Thermodynamics and kinetics, Chem. Eng. J. **322** (2017) 302–313, https://doi.org/10.1016/j.cej.2017.04.037.

[55] T. S. Anirudhan, P. G. Radhakrishnan, Thermodynamics and kinetics of adsorption of Cu(II) from aqueous solutions onto a new cation exchanger derived from tamarind fruit shell, J. Chem. Thermodyn. **40** (2008) 702–709, https://doi.org/10.1016/j.jct.2007.10.005.

[56] B. Guo, L. Chang, K. Xie, Adsorption of Carbon Dioxide on Activated Carbon, J. Nat. Gas Chem. **15** (2006) 223–229, https://doi.org/10.1016/S1003-9953(06)60030-3.

[57] X. Zhou, H. Yi, X. Tang, H. Deng, H. Liu, Thermodynamics for the adsorption of SO_2, NO and CO_2 from flue gas on activated carbon fiber, Chem. Eng. J. **200** (2012) 399–404, https://doi.org/10.1016/j.cej.2012.06.013.

[58] S. Cavenati, C. A. Grande, A. E. Rodrigues, C. Kiener, U. Müller, Metal organic framework adsorbent for biogas upgrading, Ind. Eng. Chem. Res. **47** (2008) 6333–6335, https://doi.org/10.1021/ie8005269.

[59] Z. Zhang, P. Li, T. Zhao, Y. Xia, Enhanced CO_2 Adsorption and Selectivity of CO2/N2on Amine@ZIF-8 Materials, Adsorp Sci Technol. **2022** (2022) 1-12, https://doi.org/10.1155/2022/3207986.

[60] J. A. Dunne, M. Rao, S. Sircar, R. J. Gorte, A. L. Myers, Calorimetric heats of adsorption and adsorption isotherms. 2. O_2, N_2, Ar, CO_2, CH_4, C_2H_6, and SF_6 on NaX, H-ZSM-5, and Na-ZSM-5 zeolites. Langmuir, **12** (1996) 5896-5904, https://doi.org/10.1021/la960496r.